Rayleigh-Bénard convection in binary-gas mixtures: Thermophysical properties and the onset of convection

Jun Liu and Guenter Ahlers

Department of Physics and Center for Nonlinear Science, University of California, Santa Barbara, California 93106

(Received 3 February 1997)

We present an experimental investigation of Rayleigh-Bénard convection in binary-gas mixtures. In order to interpret the results quantitatively, we determined the necessary thermodynamic and transport properties for six mixtures (He-CO$_2$, He-SF$_6$, He-Xe, Ne-Ar, Ar-CO$_2$, and H$_2$-Xe) by a combination of data from the literature, molecular-theory calculations, and thermal-conductivity measurements. All six mixtures have positive separation ratios Ψ. The Lewis number $\mathcal{L}$ (the ratio of the mass to the thermal diffusivity) is of $O(1)$, in contrast to liquid mixtures where $\mathcal{L} = O(10^{-2})$. An important feature of the gas mixtures is that their Prandtl number (the ratio of the kinematic viscosity to the thermal diffusivity) can be lower than those of the two pure components. We discuss the physical reason for this and show that the minimum Prandtl number reached by using binary-gas mixtures is about 0.16. The critical temperature difference ΔT_c for the onset of convection is determined from measurements of the Nusselt number $\mathcal{N}$ (the effective thermal conductivity) and from the contrast of shadowgraph images as a function of ΔT. The results agree well with the prediction of linear stability analysis. In contrast to convection in binary-liquid mixtures with $\Psi > 0$, $\mathcal{N}$ for the gas mixtures increases significantly with $\epsilon \equiv \Delta T/\Delta T_c - 1$ as soon as the convection starts at the Soret onset and is qualitatively similar to the Nusselt number of pure fluids. However, the critical Rayleigh number R_c is lower than the value $R_{c0} = 1708$ of pure fluids. The pattern at onset in the gas mixtures initially consists of parallel straight rolls, in contrast to binary-liquid mixtures where the pattern consists of squares. Based on the gas-mixture properties, we find that the Dufour effect (the reciprocal process of the Soret effect) is relatively weak. The slope $d\mathcal{N}/d\epsilon$ of $\mathcal{N}$ at onset is found to be consistent with that predicted by an eight-mode Galerkin truncation. [S1063-651X(97)04206-2]

PACS number(s): 47.20.Bp, 47.27.Te, 51.20.+d, 51.30.+i

I. INTRODUCTION

A quiescent horizontal fluid layer heated from below becomes unstable and undergoes a transition to buoyancy-driven convection, namely, Rayleigh-Bénard convection (RBC), when the temperature difference ΔT across it exceeds a critical value ΔT_c. This system has long been used to investigate many fundamental and practical problems [1–8]. Particularly, it has become a paradigm in the study of complex spatiotemporal behavior in spatially extended nonlinear nonequilibrium systems [6]. This is so for two reasons. On the one hand, RBC lends itself to well controlled, quantitative experiments [5,8]. On the other hand, the equations of motion of the system are well known (the Navier-Stokes equations and associated boundary conditions) and permit a close connection between theory and experiment, which has led to detailed tests of theoretical concepts [2,3,6]. There has been a large amount of experimental work on RBC in single-component liquids and gases and in binary-liquid mixtures. In this paper, we report RBC experiments in *binary-gas* mixtures and show that they open an alternative parameter range with different opportunities in the study of RBC.

The primary control parameter for RBC is the Rayleigh number

$$R \equiv \frac{\alpha g d^3 \Delta T}{\kappa \nu},$$ (1)

a dimensionless measure of the temperature difference across the fluid layer. Here

$$\alpha \equiv -(1/\rho)(\partial\rho/\partial T)_P$$ (2)

is the isobaric thermal expansion coefficient (ρ is the density and P the pressure), g the acceleration of gravity, d the fluid-layer thickness, κ the thermal diffusivity, and ν the kinematic viscosity. As R increases from zero, the destabilizing density gradient (or buoyancy force) increases. Convection occurs when R exceeds a critical value R_c (ΔT exceeds ΔT_c). For a single-component fluid, the critical Rayleigh number (corresponding to $\Delta T = \Delta T_{c0}$) is $R_{c0} = 1708$, independent of material properties, and the convection just above onset consists of stationary rolls. When R increases further above R_c, various flow patterns and time dependences evolve [5,9–12], and turbulence appears at very large R [7].

The nonlinear behavior of convection above R_c depends on the Prandtl number

$$\sigma \equiv \nu/\kappa$$ (3)

as well as on R. Although σ does not affect the onset of convection, it has important effects on secondary instabilities of the convection-roll patterns. For the idealized case of infinitely extended parallel straight rolls, Busse and collaborators [2,13–15] have determined the main features of these instabilities as well as their boundaries as a function of R, σ, and the roll wave number k. These predictions describe fairly well also the case of convection in large but finite samples when σ is large. However, for low σ experiments have revealed complex spatiotemporal behavior at R slightly above R_c [5,12,16–18], where straight rolls are predicted to

be stable in the infinite system. To a large extent this time dependence of the patterns is associated with roll curvature induced by the sidewalls of the cell, which leads to large-scale flows. These flows in turn create a wave-number distribution that, for small σ, overlaps the stability boundaries of the infinite system [5,12].

Another parameter relevant to experiments is the lateral extent of a convection cell, as described by the aspect ratio

$$\Gamma \equiv r/d, \qquad (4)$$

where r is the radius for a cylindrical cell. When the system is small ($\Gamma \lesssim 3$), RBC can exhibit temporal chaos [6,19,20] as R increases from R_c, and the spatial dependence is dynamically unimportant. For large Γ, the spatial degrees of freedom play an important role in the complex evolution of convection patterns, resulting in spatiotemporal chaos [5,17,18,21–24]. Recently it was shown that the onset of spiral-defect chaos, a spatiotemporal chaos occurring only for $\Gamma \gg 1$ and low σ, depends significantly on the aspect ratio [17,18,23,25].

The nature of Rayleigh-Bénard convection in pure fluids is determined by the above three dimensionless numbers when the Oberbeck-Boussinesq approximation [26–28] applies. In this approximation it is assumed that the variations of all fluid properties with temperature (except for the density in the buoyancy force) can be neglected. For most of the work reported in this paper this approximation is very good.

For binary mixtures, additional parameters are required to describe the nature of the convecting state because of the coupling between concentration and temperature fields. This coupling results in new phenomena that do not occur in pure fluids, including traveling waves, localized pulses, time-dependent envelopes of the convection rolls, and square patterns [29–31]. In binary mixtures, temperature gradients change the concentration field because of thermal diffusion [32,33]. This so-called Soret effect is characterized in RBC by the separation ratio

$$\Psi \equiv -\frac{\beta}{\alpha}\frac{k_T}{T} = -\frac{\beta}{\alpha}C(1-C)S_T, \qquad (5)$$

where β is the solutal expansion coefficient, k_T the thermal diffusion ratio [34], T the temperature, C the mass concentration of the heavier component [see Eq. (14) below], and $S_T = k_T/C(1-C)T$ the Soret coefficient. The quantity k_T is defined so that the heavier component moves to the cold (hot) region when $k_T > 0$ ($k_T < 0$). The thermal expansion coefficient α [Eq. (2)] is computed at constant C and

$$\beta \equiv -(1/\rho)(\partial\rho/\partial C)_{P,T}. \qquad (6)$$

When $\Psi < 0$, the induced concentration gradient stabilizes the conduction state because the heavy component moves to the hot region and retards the buoyancy. Thus the critical Rayleigh number is elevated, i.e., $R_c > R_{c0}$. On the other hand, when $\Psi > 0$, the induced concentration gradient is destabilizing the conduction state and the critical Rayleigh number is reduced, i.e., $R_c < R_{c0}$.

In binary mixtures, the dynamics of the concentration variable is associated with an independent time scale governed by the concentration diffusivity D. Thus the Lewis number

$$\mathcal{L} \equiv D/\kappa \qquad (7)$$

is an important parameter that measures the ratio of the thermal-diffusion time to the mass-diffusion time. For liquid mixtures, $\mathcal{L}$ is small [$O(10^{-2})$]. In that case it is possible for the concentration to temporally lag behind the thermal gradient. When $\Psi < 0$, this can lead to oscillations that are responsible for the existence of traveling waves and other interesting phenomena [29]. On the other hand, for $\Psi > 0$, the convection is stationary and the pattern that forms for small $\mathcal{L}$ is one of squares [30,31,35]. Mass diffusion carries little heat for small $\mathcal{L}$ and thus for $\Psi > 0$ the heat transport is not significantly enhanced by the convection for $R_c < R < R_{c0}$ [30,31], where the Soret mechanism dominates. In binary-gas mixtures, however, $\mathcal{L} = O(1)$ and the heat transport is enhanced significantly in the range $R_c < R < R_{c0}$, as we will show in this paper. The pattern immediately above R_c then consists of rolls like those in pure fluids.

The coupling of temperature and concentration in binary mixtures also gives rise to the Dufour effect, which consists of temperature gradients induced by concentration gradients. It is the reciprocal process of the Soret effect in Onsager's linear reciprocal relations [32,36,37]. Recently, Lücke and co-workers [37,38] carried out a theoretical study of the role of the Dufour effect in RBC. A dimensionless Dufour number [37] was defined as

$$Q \equiv \frac{T\alpha^2}{c_p\beta^2}\left(\frac{\partial\mu}{\partial C}\right)_{P,T}, \qquad (8)$$

where $\mu(P,T,C)$ is the chemical-potential difference per unit mass [see Eq. (24) below] and c_p is the isobaric specific heat per unit mass. Note that Q is a purely thermodynamic quantity. The coupling strength of the Dufour effect depends on combinations of Q, $\mathcal{L}$, and Ψ [see Eq. (10) below]. In liquid mixtures, $\mathcal{L}$ is small and thus the Dufour effect is negligible [36,37]. On the other hand, in gas mixtures, $\mathcal{L} = O(1)$ and the Dufour effect may not necessarily be ignored. When the effect is strong, it can significantly change the bifurcation topology and the existence regimes of stationary and traveling-wave convection [37,38].

In order to understand the relevance of the Dufour effect more quantitatively, we examine the various terms in the governing equations [2,37,39] for RBC in binary mixtures. Scaling lengths by d, time by d^2/κ, temperature by $\kappa\nu/\alpha g d^3$, concentration by $\kappa\nu/\beta g d^3$, and P/ρ by κ^2/d^2, the Oberbeck-Boussinesq approximation leads to [37]

$$\frac{1}{\sigma}(\partial_t + \mathbf{v}\cdot\nabla)\mathbf{v} = -\nabla\Pi + (\theta+c)\hat{\mathbf{z}} + \nabla^2\mathbf{v}, \qquad (9)$$

$$(\partial_t + \mathbf{v}\cdot\nabla)\theta = R\mathbf{v}\cdot\hat{\mathbf{z}} + (1 + \mathcal{L}Q\Psi^2)\nabla^2\theta - \mathcal{L}Q\Psi\nabla^2 c, \qquad (10)$$

$$(\partial_t + \mathbf{v}\cdot\nabla)c = R\Psi\mathbf{v}\cdot\hat{\mathbf{z}} + \mathcal{L}\nabla^2(c - \Psi\theta), \qquad (11)$$

TABLE I. Primary thermophysical properties of pure gases and binary-gas mixtures. The quantity X denotes the mole fraction of the heavier component in a mixture.

Property	Pure gas	Binary-gas mixture
density	$\rho(P,T)$	$\rho(P,T,X)$
shear viscosity	$\eta(P,T)$	$\eta(P,T,X)$
thermal conductivity	$\lambda(P,T)$	$\lambda(P,T,X)$
isobaric specific heat (per mole)	$C_p(P,T)$	$C_p(P,T,X)$
mass diffusivity		$D(P,T,X)$
thermal diffusion ratio		$k_T(P,T,X)$
chemical-potential difference [a]		$\mu(P,T,X)$

[a]See Eq. (24) for the definition.

where $\theta(x,y,z)$, $c(x,y,z)$, and $p(x,y,z)$ are the deviations of T, C, and P from their values in the conduction state. Here x and y are the horizontal axes, z is the vertical axis opposite the direction of gravity, and $\hat{\mathbf{z}}$ is the unit vector along z. The Dufour effect changes the temperature-field equation [Eq. (10)] both ''diagonally'' via $\mathcal{L}Q\Psi^2\nabla^2\theta$ and ''off diagonally'' via $-\mathcal{L}Q\Psi\nabla^2 c$. Thus a significant Dufour effect should occur when the parameter combinations $\mathcal{L}Q\Psi^2$ and/or $\mathcal{L}Q\Psi$ are sufficiently large. Although Linz [40,41] and Hort *et al.* [37] roughly estimated the parameters for binary-gas mixtures, there has been no direct assessment of the Dufour effect for any *real* gas mixtures because a complete set of thermophysical properties is rarely documented. In this paper, we determine all the necessary properties for several binary-gas mixtures with good accuracy. It turns out that the role of the Dufour effect in all of these is very minor. The reason for this is that Ψ tends to be small when Q is large. We test the predictions of linear [37] and weakly nonlinear [38] theory based on the above equations by measuring the critical Rayleigh number R_c, the critical wave number k_c, and the Nusselt number $\mathcal{N}$ near onset.

One can see from Eqs. (9)–(11) that the Prandtl number σ determines the relative weight of the nonlinear terms $\mathbf{v}\cdot\nabla\mathbf{v}$, $\mathbf{v}\cdot\nabla\theta$, and $\mathbf{v}\cdot\nabla c$. The stability and evolution of convection patterns depend greatly on which nonlinear terms are dominant. The term $\mathbf{v}\cdot\nabla\mathbf{v}$ can yield a vertical-vorticity field [5,42] giving rise to large-scale horizontal flows, whose magnitude is *inversely* proportional to σ. It has been shown theoretically [42–45] and experimentally [46,47] that the large-scale flows are responsible for much of the complex spatiotemporal behavior of convection patterns observed at low Prandtl numbers [5,12,16–18]. Thus it is of great interest to investigate the role of σ *quantitatively*, especially for $\sigma\lesssim 1$. However, as a material property, σ cannot be readily adjusted in a given experiment. Prandtl numbers of pure gases generally are larger than the value 2/3 derived from kinetic theory for rigid-sphere molecules [48]. Liquid metals have $\sigma\lesssim 0.03$, but we know of no classical pure fluids [49] with $0.03\lesssim\sigma\lesssim 0.67$. Employing simplified models, Giacobbe [50] estimated the Prandtl number for binary noble-gas mixtures involving helium and found that σ can reach about 0.2 for a helium-xenon mixture. In the present paper, we use a more accurate method, based on a combination of statistical-mechanical theory and experimental data from the literature and our experiments, to show that σ as low as 0.16 can be achieved by a hydrogen-xenon mixture. In our experiments we cover the range $0.16\lesssim\sigma\lesssim 1.00$ by using different

binary-gas mixtures and pure gases and by changing their pressures and concentrations. Some results for the effect of the Prandtl number on spiral-defect chaos have been reported in Ref. [25] and we plan to present more detailed results in another paper [51].

The rest of this paper is organized as follows. In Sec. II we describe the general method used to obtain the thermophysical properties of pure gases and binary-gas mixtures required in the study of RBC. We also explain why Prandtl numbers can be lowered in binary-gas mixtures with a simple model. Section III presents the experimental setup and measurement methods. Experimental results for the onset of convection are presented in Sec. IV. Finally, in Sec. V we discuss the relative importance of the Soret and Dufour effects in binary-gas mixtures and give a summary of our work.

II. THERMOPHYSICAL PROPERTIES OF BINARY-GAS MIXTURES

Under ideal circumstances the physical properties of gases and their mixtures would be based on experimental determinations. Unfortunately, the amount of experimental data required for our needs is formidable and we must resort to less satisfactory approaches. Whenever possible, we used experimental measurements. When these were inadequate, we employed theoretical estimates based on kinetic theory and empirical interpolation formulas. This approach does not lend itself to a systematic presentation because the details vary from case to case. Thus, in this section we attempt to present the general methods that we have used. The details will differ for different mixtures, and more specific information including references to the literature for each of them is presented in the Appendix.

To study RBC in gases quantitatively, we need to know the ''primary'' thermophysical properties listed in Table I. Other thermodynamic and transport coefficients derivable from them are the kinematic viscosity $\nu=\eta/\rho$, the thermal diffusivity $\kappa=\lambda/\rho c_p$, the thermal and solutal expansion coefficients given by Eqs. (2) and (6), and the specific heat per unit mass $c_p=C_p/M$. Here

$$M=M_2 X+M_1(1-X) \tag{12}$$

is the molar mass of the mixture and M_1 and M_2 are the molar masses of the lighter and heavier pure component, respectively. The mole fraction X of the heavier component is given by

$$X = N_2/(N_1 + N_2), \qquad (13)$$

where N_1 and N_2 are the number of moles of the lighter and heavier component, respectively. In the hydrodynamic equations the mass concentration often is used and it is given by

$$C = N_2 M_2/(N_1 M_1 + N_2 M_2). \qquad (14)$$

The relationship between X and C is easily derived to be

$$C = X M_2/M \qquad (15)$$

and the derivative dC/dX is given by

$$dC/dX = M_1 M_2 (N_1 + N_2)^2/(N_1 M_1 + N_2 M_2)^2. \qquad (16)$$

We wrote a series of programs to calculate the thermophysical properties of eight pure gases (He, Ne, Ar, Xe, H_2, N_2, CO_2, and SF_6) and six binary-gas mixtures (He-Xe, He-CO_2, He-SF_6, Ne-Ar, Ar-CO_2, and H_2-Xe) as a function of temperature and pressure. Using the same procedure, it is possible to determine thermophysical properties for many other binary-gas mixtures, especially noble-gas mixtures. The properties calculated in this work are applicable to the range $0°-60\,°C$ and $1-50$ bars, except that the partial pressure has to be lower than 22 bars for SF_6 and 30 bars for Xe.

For the eight pure gases, their properties have been well summarized in the literature as functions of pressure and temperature (e.g., see Refs. [52–55]). On the other hand, despite voluminous work [56,57], the thermophysical properties are documented incompletely for the mixtures. Fortunately, considerable success has been achieved in calculating the equation of state and the transport properties of dilute gases and gas mixtures from statistical mechanics, using a combination of the principle of corresponding states with intermolecular potentials based on a limited, well-chosen set of accurate measurements [32,58–61]. Such calculations have reproduced the properties of some pure gases and gas mixtures with an accuracy comparable to measurements. Because the theoretical equations and empirical collision integrals that we used are complicated and have been documented in Refs. [32,59–61], we do not reproduce them here. In this work, while the pure gas properties were mainly obtained by fitting literature data, the mixture properties were determined by a combination of fitting data in the literature, doing molecular theory calculations, and measuring the thermal conductivity ourselves.

A. General procedure

1. Density

The density $\rho(P,T,X)$ is calculated from the equation of state

$$Pv/RT = 1 + B(T,X)/v + C(T,X)/v^2 + D(T,X)/v^3 + \cdots, \qquad (17)$$

where v is the molar volume, R the gas constant, and $B(T,X)$, $C(T,X)$, ... the second, third, etc., virial coefficients. For our eight pure gases, the equations of state have been summarized in the literature, some up to the eighth or ninth virial coefficient. For a binary-gas mixture, the second virial coefficient is

$$B(T,X) = (1-X)^2 B_1(T) + 2X(1-X)B_{12}(T) + X^2 B_2(T), \qquad (18)$$

where B_1 and B_2 are the second virial coefficients of components 1 and 2, respectively, and B_{12} the second *interaction* virial coefficient associated with the unlike pair interaction between components 1 and 2. The coefficient $B_{12}(T)$ has been measured for many mixtures [62–66] and can be calculated by statistical-mechanical theory for some of them [59,61]. The third virial coefficient is sometimes necessary to improve the accuracy of mixture densities, but the third unlike interaction virial coefficients are seldom available. So the third virial coefficients of pure gases were used to evaluate $C(T,X)$ approximately.

2. Viscosity, thermal conductivity, and heat capacity

For both physical reasons and practical purposes, $\eta(\rho,T,X)$ and $\lambda(\rho,T,X)$ are expressed as a sum of two independent contributions [32,67]. Thus, writing $Y(\rho,T,X)$ for both properties we have

$$Y(\rho,T,X) = Y_0(T,X) + \Delta Y(\rho,T,X). \qquad (19)$$

Here $Y_0(T,X) = Y(0,T,X)$ is the contribution to the transport property in the limit of zero density, where only two-body molecular interactions occur. The second term $\Delta Y(\rho,T,X)$ represents the contribution of all other effects to the transport property at elevated densities, such as many-body collisions and collisional transfer. It can be expanded as a polynomial of ρ,

$$\Delta Y(\rho,T,X) = Y_1(T,X)\rho + Y_2(T,X)\rho^2 + Y_3(T,X)\rho^3 + \cdots. \qquad (20)$$

The expansion (20) is usually kept up to the second or third term. For the relatively narrow temperature range used in our experiment, $Y_1(T,X)$, $Y_2(T,X)$, etc., are sometimes assumed to be temperature independent, depending on the data available to us. Similarly, the heat capacity $C_p(\rho,T,X)$ can also be expressed as Eq. (19) [32], where the first term is then due to the molecule's translational, rotational, and vibrational degrees of freedom and the second term stands for the contribution of all intermolecular interactions. For the pure gases used in our experiment, η, λ, and C_p are tabulated in the literature and easily can be fitted to Eqs. (19) and (20).

For the binary-gas mixtures, the calculation of η and λ is much more complicated. Different methods have to be chosen, depending on the available data and theoretical results. For the noble-gas mixtures Ne-Ar and He-Xe, the zero-density viscosity η_0 and the zero-density thermal conductivity λ_0 can be calculated from kinetic theory and empirical integrals given by Kestin *et al.* [59] with an accuracy of 1% or so. For the mixtures involving polyatomic molecules, although η_0 can be calculated from kinetic theory [61,68], the thermal conductivity cannot be treated well by kinetic theory due to the internal degrees of freedom and anisotropic pair potentials. When there are enough reliable experimental data, such as for He-CO_2 and Ar-CO_2, both η_0 and λ_0 were obtained by fitting to the data the empirical expression [56,69,70]

$$Y_0 = \frac{Y_{01}}{1 + A_{12}X/(1-X)} + \frac{Y_{02}}{1 + A_{21}(1-X)/X}, \quad (21)$$

where Y_{01} and Y_{02} are the zero-density values of the pure components and A_{12} and A_{21} are adjustable parameters. In the case of H_2-Xe and He-SF_6, we did not find enough data to apply Eq. (21). Thus the kinetic-theory equations and empirical integrals documented in Ref. [61] were used to calculate η_0 for He-SF_6, while the equations and integrals based on the Lennard-Jones potential summarized in Ref. [68] had to be employed to determine η_0 for H_2-Xe. An approximate method due to Monchick et al. [71,72], which was summarized later in Ref. [73], was used to estimate λ_0 for H_2-Xe and He-SF_6. This method relates the mixture thermal conductivity to the thermal conductivity of its components and other properties of the system such as the viscosity and diffusion constants, which can be predicted accurately by kinetic theory. To get a good estimation of λ_0, these properties were obtained from experimental data whenever possible. Because the method may have relatively large errors, the final result of λ was checked by our own measurements. We show later that the approximate method can predict λ quite accurately for He-SF_6, but gives a result slightly smaller than the measured one for H_2-Xe. In order to obtain the pressure dependence of the mixture η and λ, we fitted Eq. (20) to experimental data whenever possible. When no data are available, we added the contributions of the two pure components together, i.e., $\Delta Y(\rho,T,X) = \Delta Y_1(\rho_1,T) + \Delta Y_2(\rho_2,T)$, where ρ_1 and ρ_2 are the densities of two components in the mixture and $\rho_1 + \rho_2 = \rho$. Since the pressure dependence of η and λ is usually small in our pressure range, such an approximation should work well.

Because the specific heat of a gas is mainly contributed by the molecule's translational, rotational, and vibrational degrees of freedom, we assumed the contribution of unlike interactions of components 1 and 2 to be negligible. Hence we calculated the mixture heat capacity by adding the contributions of the two components together [50,70]:

$$C_p(P,T,X) = (1-X)C_{p1}(P_1,T) + XC_{p2}(P_2,T), \quad (22)$$

where P_1 and P_2 are the partial pressures of components 1 and 2, respectively.

3. Diffusion constant and thermal diffusion ratio

The mass diffusivity D and the zero-density thermal diffusion ratio k_{T0} are given by kinetic theory [32,59,61]. The theory predicts that the product PD is constant for dilute gases. Hence, in studying the pressure dependence of D, the product PD should be studied. To first order, the pressure dependence of both PD and k_T can be written as [74–77]

$$Z(P,T,X) = Z_0(T,X)[1 + B_Z(X,T)P], \quad (23)$$

where $Z(P,T,X)$ stands for both PD and k_T, and $Z_0(T,X)$ for their zero-pressure values. The second ''virial coefficient'' $B_Z(T,X)$ is a function of concentration and temperature. Unfortunately, there are only limited data on the pressure dependence of k_T and PD. We used the measurements of $B_{k_T}(T,X)$ for He-CO_2 and He-SF_6 by Trengove et al. up to 5 atm [76] and employed approximate methods summa-
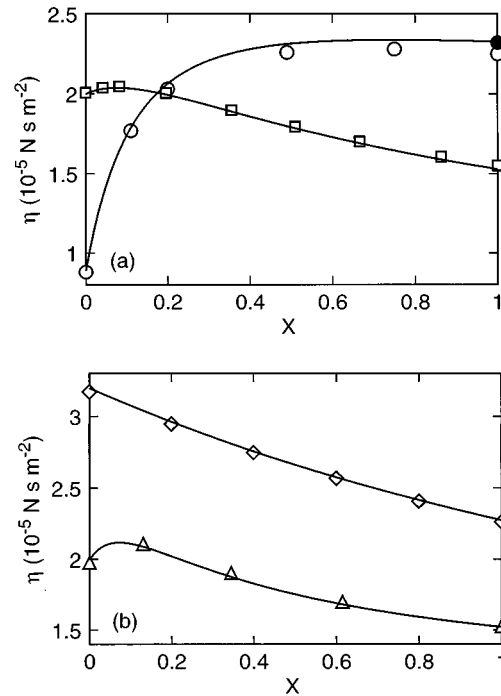

FIG. 1. Shear viscosity η as a function of the mole fraction X of the heavy component in binary mixtures. The symbols are experimental data and the curves are the results calculated from the fits used in this work at the corresponding P and T. (a) The open circles [78] are for H_2-Xe at $P=1.0$ bar and $T=23$ °C, the solid circle [53] is for pure Xe at the same condition, and the squares [79] are for He-CO_2 at $P=23.3$ bars and $T=30$ °C. (b) The triangles [80] are for He-SF_6 at $P=1.0$ bar and $T=25$ °C and the diamonds [81] are for Ne-Ar at $P=1.0$ bar and $T=25$ °C.

rized in Refs. [74,75] and in Refs. [76,77] to calculate $B_D(T,X)$ and $B_{k_T}(T,X)$, respectively, from the second virial coefficients of pure gases and mixtures. Dunlop and his collaborators [74–76] have tested these methods experimentally for several mixtures at relatively low pressures (up to 5 atm for k_T and 9 atm for PD). However, the second virial coefficient $B_{k_T}(X,T)$ may not be sufficient because of the strong pressure dependence of k_T.

Finally, we point out that the value of k_T depends on which concentration one uses, the mole fraction X or the mass concentration C. The original definition of k_T [34] is based on the mole fraction; however, the mass concentration is used in the governing equations and the separation ratio. The two values of k_T are converted from one to another by $k_{T,mass} = (dC/dX)k_{T,mole}$, where (dC/dX) is given by Eq. (16).

4. Chemical potential

The chemical-potential difference per unit mass of the mixture $\mu(P,T,C)$ is given by [39]

$$\mu = \mu_2/M_2 - \mu_1/M_1, \quad (24)$$

where μ_1 and μ_2 are the chemical potentials per mole of the single components. Assuming the mixtures are ideal gases [37], we have
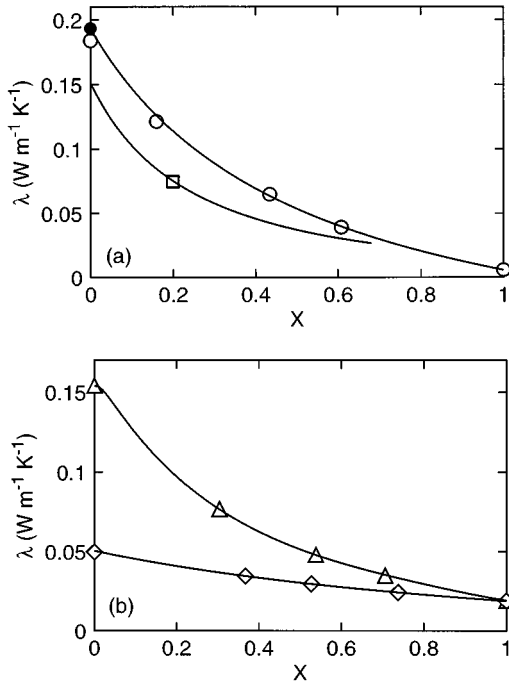
FIG. 2. Thermal conductivity λ as a function of the mole fraction X. The symbols are experimental data and the curves are the results calculated from the fits used in this work at the corresponding P and T. (a) The open circles [82] are for H_2-Xe at $P=0.2$ bar and $T=40$ °C, the solid circle [83] is for pure H_2 at the same condition, and the square (our measurement) is for He-SF_6 at $P=28.1$ bars and $T=20.5$ °C. (b) The triangles [84] are for He-CO_2 at $P=28.5$ bars and $T=27.5$ °C and the diamonds [85] are for Ne-Ar at $P=31.0$ bars and $T=27.5$ °C.

$$\mu_i = f_i(P,T) + RT\ln\frac{N_i}{N_1+N_2} \qquad (25)$$

for $i=1$ and 2. Then

$$\left(\frac{\partial\mu}{\partial C}\right)_{T,P} = \frac{RT}{C(1-C)[CM_1+(1-C)M_2]}, \qquad (26)$$

which is used to calculate the Dufour number [Eq. (8)]. The quantity $(\partial\mu/\partial C)_{T,P}$ becomes infinite when C approaches 0 or 1.

5. Accuracy of the calculation

We estimated the accuracy of the above calculations by comparing the results with literature data and our own measurements of λ for the mixtures. For the pure gases, the estimated accuracy is better than 2% for all properties (ρ, η, λ, and C_p). For the six binary mixtures, the estimated accuracies are about 2% for ρ and η, 2–5 % for λ, 4–7 % for D, and 5–10 % for k_{T0}. The accuracy is better for noble-gas mixtures than for mixtures involving polyatomic molecules. Because of the strong pressure dependence of k_T and the lack of data at elevated pressures, the accuracy of k_T is relatively poor. There are no experimental data for C_p, but we estimated that its accuracy is within 5% for the relatively low pressures used in this experiment.
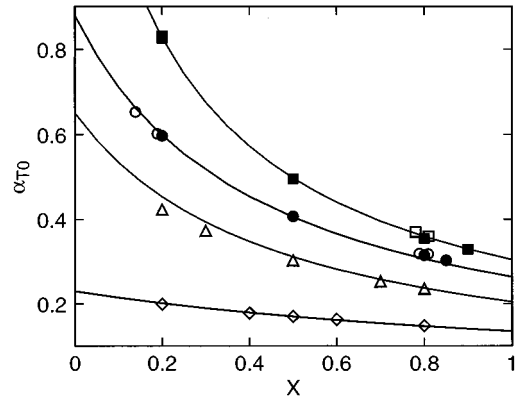
In Figs. 1–3 we present several examples of the shear

FIG. 3. Reduced low-density thermal-diffusion ratio α_{T0} as a function of the mole fraction X. The symbols are experimental data, and the curves are calculated from the fits used in this work at the corresponding T. Open [86] and solid [76] squares, He-SF_6 at $T=26.85$ °C; open [87] and solid [76] circles, He-CO_2 at $T=26.85$ °C; triangles [88], H_2-Xe at $T=26.85$ °C; diamonds [89], Ne-Ar at $T=21.85$ °C.

viscosity η, the thermal conductivity λ, and the *reduced* low-density thermal diffusion ratio $\alpha_{T0}=k_{T0,mole}/X(1-X)$ as functions of X. To compare with experimental data, the calculations were done at the pressures and temperatures of those experiments cited in the figures. The results agree with the experiments within the accuracies given above. It is interesting to note the agreement between our measured λ and the calculated one for He-SF_6 in Fig. 2(a). The measurement method of λ and more comparisons are given in Sec. III D.

B. Dimensionless numbers

Now we can calculate the four dimensionless material properties required in the study of RBC in binary-gas mixtures, namely, the separation ratio Ψ, the Lewis number $\mathcal{L}$, the Dufour number Q, and the Prandtl number σ. In Figs. 4–7 these parameters are presented as functions of the mole fraction X of the heavy component for $P=22$ bars and $T=25$ °C. The separation ratio Ψ for all six mixtures is *posi-*
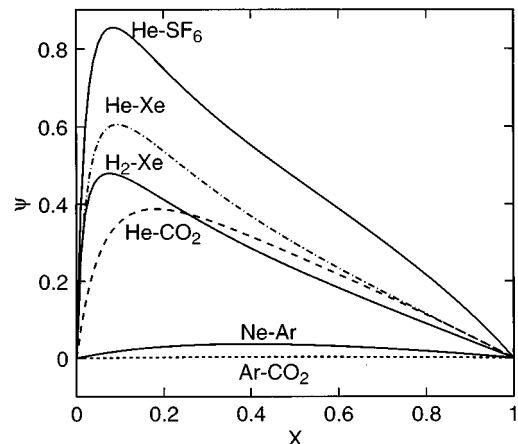

FIG. 4. Separation ratio Ψ as a function of the mole fraction X of the heavy component for $P=22$ bars and $T=25$ °C.
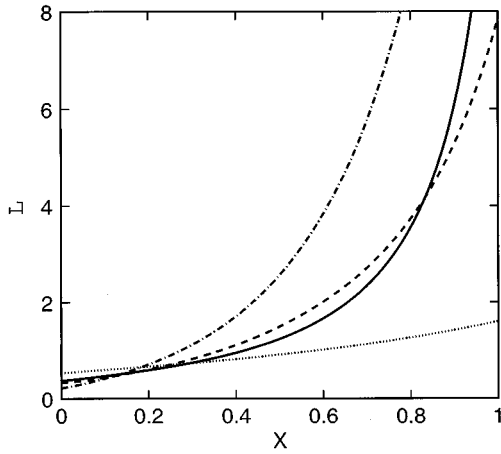
FIG. 5. Lewis number $\mathcal{L}$ as a function of the mole fraction X of the heavy component. Solid line, H_2-Xe; dashed line, He-CO_2; dot-dashed line, He-SF_6; dotted line, Ne-Ar. To improve the clarity of this figure, we do not plot the results for Ar-CO_2 and He-Xe, which are close to those of Ne-Ar and H_2-Xe, respectively. For these data $P=22$ bars and $T=25\,°C$.

tive (Fig. 4) and goes to zero at $X=0$ and 1 [Eq. (5)]. The maximum value Ψ_{max} is strongly affected by the molar-mass ratio

$$\mathcal{M}=M_2/M_1 \qquad (27)$$

(Table II). If $\mathcal{M}$ is close to one, the separation ratio is small, e.g., Ψ_{max} is only 3.2×10^{-3} for Ar-CO_2. However, when $\mathcal{M}\gg1$, the separation ratio can be quite large, as in the case of He-SF_6, where $\Psi_{max}\simeq0.85$. The peak position of $\Psi(X)$ shifts to low X as $\mathcal{M}$ increases. In the case of noble-gas mixtures, the separation ratio increases monotonically with $\mathcal{M}$ at fixed X. Linz noted similar behavior in a previous analysis of Lorentz-gas mixtures [41]. This monotonic relation does not hold well for binary-gas mixtures involving polyatomic molecules (Fig. 4).

The Lewis numbers increase with X from minimum values between 0.2 and 0.7 near $X=0$ to maximum values between 1.6 and 22 near $X=1$ (Fig. 5). The maximum value is 22 for He-SF_6 and 13.7 for H_2-Xe. On the other hand, the Dufour number is proportional to $1/C(1-C)$ [Eq. (26)] and thus diverges in the pure-gas limits (Fig. 6). The *minimum* value of $Q(X)$ is about 34 for Ar-CO_2 and 3.2 for Ne-Ar, but Q is close to zero for the other four mixtures with $\mathcal{M}>10$ except near the pure-gas limits (Fig. 6). More inter-

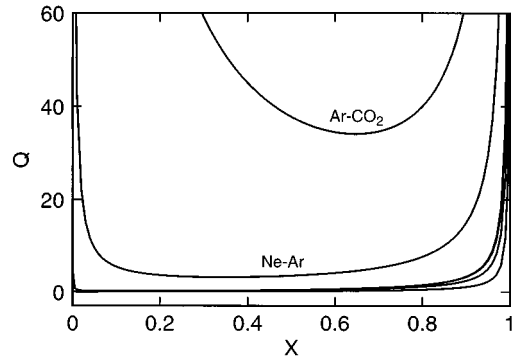FIG. 6. Dufour number Q as a function of the mole fraction X of the heavy component. The curves that are not labeled are for H_2-Xe, He-Xe, He-CO_2, and He-SF_6 from top to bottom. The curves for H_2-Xe and He-Xe are nearly the same. For these data $P=22$ bars and $T=25\,°C$.

estingly, for all mixtures except Ar-CO_2, the Prandtl number is lower than that of either pure component over most of the range of X (Fig. 7). The minimum value of σ decreases almost monotonically with increasing $\mathcal{M}$ as shown in Table II.

One sees from Figs. 4 and 6 and Table II that Ψ and Q do not *both* have large values under the same conditions. Since the strength of the Dufour effect depends on $\mathcal{L}Q\Psi$ and $\mathcal{L}Q\Psi^2$ [Eq. (10)], we plotted these two parameter combinations vs X for Ar-CO_2 and He-SF_6 in Fig. 8. The values of both $\mathcal{L}Q\Psi$ and $\mathcal{L}Q\Psi^2$ are so small for Ar-CO_2 that the Dufour effect is very weak even though Q is large. For He-SF_6, the value of $\mathcal{L}Q\Psi^2$ is small, but $\mathcal{L}Q\Psi$ can be relatively large. Hence it is not straightforward to determine the strength of the Dufour effect for this mixture without additional analysis. Therefore, we discuss the influence of the Dufour effect on the onset of convection in detail in Sec. V A.

C. Why is the Prandtl number lowered in binary-gas mixtures?

It is worthwhile to understand why the Prandtl number is lowered in binary-gas mixtures. This may be useful also in design engineering involving heating or refrigeration systems [50,90], where reducing σ may increase the heat-transfer coefficient. Kinetic theory for rigid-sphere molecules [48] predicts $\eta=a(MT)^{1/2}/\delta^2\Omega$ and $\lambda=b(T/M)^{1/2}/\delta^2\Omega$, where a and b are constants, δ is the molecular diameter,

TABLE II. Molar-mass ratio $\mathcal{M}=M_2/M_1$ and minimum Prandtl number σ_{min} of six binary-gas mixtures. The values of Ψ, $\mathcal{L}$, and Q at $X=0.5$ are also shown. For these examples $T=25\,°C$ and $P=22$ bars.

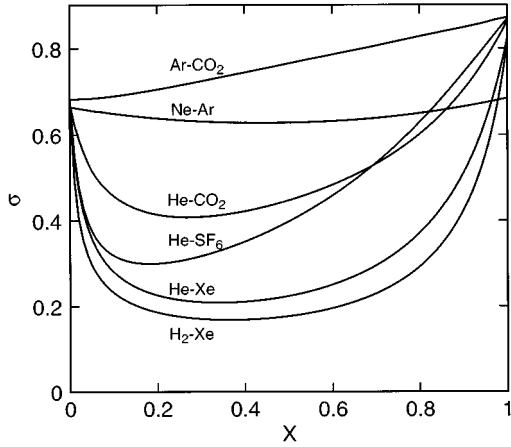| Mixture	$\mathcal{M}$	σ_{min}	Dimensionless properties at $X=0.5$		
			Ψ	$\mathcal{L}$	Q
Ar-CO_2	1.1	0.683	0.0032	1.085	37.82
Ne-Ar	2.0	0.628	0.035	0.912	3.519
He-CO_2	11.0	0.408	0.268	1.496	0.395
He-Xe	32.8	0.209	0.299	1.285	0.427
He-SF_6	36.5	0.300	0.470	2.565	0.166
H_2-Xe	65.1	0.168	0.232	1.238	0.357

FIG. 7. Prandtl number σ as a function of the mole fraction X of the heavy component. For these data $P=22$ bars and $T=25$ °C.

and Ω is a collision integral. For a monatomic gas, $c_p=(5/2)R/M$ and $\sigma=(\eta/\lambda)c_p=2/3$. Using a mole-fraction-weighting (MFW) approximation, Giacobbe [50] found

$$\eta=a\frac{(1-X)(M_1T)^{1/2}+X(M_2T)^{1/2}}{(1-X)\delta_1^2\Omega_1+X\delta_2^2\Omega_2} \qquad (28)$$

and

$$\lambda=b\frac{(1-X)(T/M_1)^{1/2}+X(T/M_2)^{1/2}}{(1-X)\delta_1^2\Omega_1+X\delta_2^2\Omega_2} \qquad (29)$$

for binary noble-gas mixtures. The mixture heat capacity is also $c_p=(5/2)R/M$, with M given by Eq. (12). Then the Prandtl number is

$$\sigma=\frac{2}{3}\frac{(1-X)+X\mathcal{M}^{1/2}}{[(1-X)+X/\mathcal{M}^{1/2}][(1-X)+X\mathcal{M}]}. \qquad (30)$$
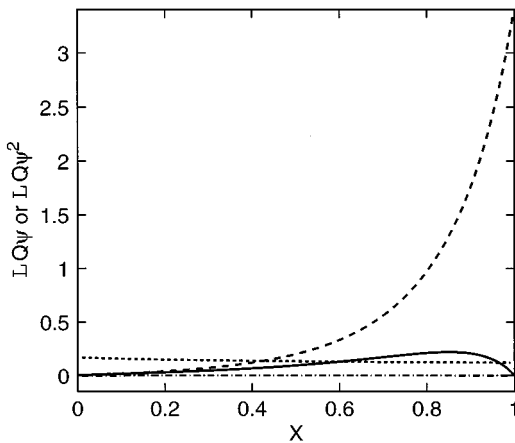

FIG. 8. Coefficients of the Dufour effect in Eq. (10), $\mathcal{L}Q\Psi$ and $\mathcal{L}Q\Psi^2$, for He-SF$_6$ and Ar-CO$_2$. Solid line, $\mathcal{L}Q\Psi^2$ for He-SF$_6$; dashed line, $\mathcal{L}Q\Psi$ for He-SF$_6$; dot-dashed line, $\mathcal{L}Q\Psi^2$ for Ar-CO$_2$; dotted line, $\mathcal{L}Q\Psi$ for Ar-CO$_2$. For these examples $P=22$ bars and $T=25$ °C.
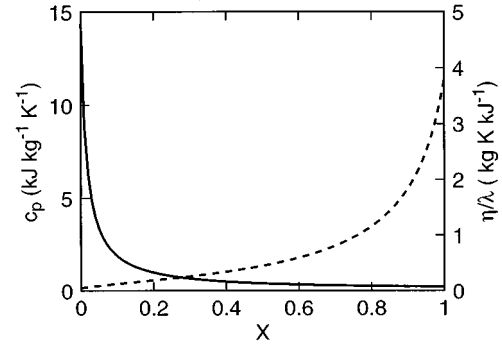

FIG. 9. Ratio η/λ (dashed curve) and the heat capacity per unit mass c_p (solid curve) as a function of X for He-SF$_6$. For this example $P=22$ bars and $T=25$ °C.

It can be shown analytically that the denominator in Eq. (30) is larger than the numerator for $0<X<1$ if $\mathcal{M}>1$. The denominator equals the numerator for pure gases ($X=0,1$). A larger value of $\mathcal{M}$ yields a smaller value of σ for a fixed X. Therefore, the Prandtl number of binary-gas mixtures is always smaller than that of pure gases for a rigid-sphere model. The smallest value of σ decreases with increasing $\mathcal{M}$. This argument can be extended to binary-gas mixtures involving polyatomic molecules by employing the Eucken correction [48] in the estimate of the thermal conductivity of polyatomic gases. For two pure components $\eta/\lambda\propto M$, so the ratio is small for the light component and large for the heavy one. Since the square roots of the molar masses enter into η/λ, the ratio grows relatively slowly as X increases until X is close to one (see Fig. 9 for an example of a real gas mixture). However, in the *mass* heat capacity c_p, the mass of the heavy molecule is more important and c_p drops quickly as X increases from 0 and then begins to level off (Fig. 9). Hence the product of η/λ and c_p reaches a minimum at a middle value of X.

In Fig. 10 we compare the estimates based on the MFW approximation with our numerical results for $P=1$ bar and $T=25$ °C for four mixtures. In the case of a monatomic (noble) gas mixture, the MFW method predicts a minimum value of σ very close to the real value, but at a somewhat different concentration [Fig. 10(a)]. In the case of mixtures involving polyatomic gases [Fig. 10(b)], two MFW curves are shown for each mixture: the dashed curve assumes a polyatomic molecule to be a monatomic one having the same mass, while the dot-dashed curve takes the internal degrees of freedom into account when estimating the thermal conductivity and heat capacity. It is apparent that the internal degrees of freedom increase the minimum Prandtl number. The increase is more significant when a polyatomic molecule consists of a larger number of atoms. For example, the molar-mass ratio $\mathcal{M}$ of He-SF$_6$ is larger than that of He-Xe, but its minimum σ is considerably higher than that of He-Xe (Fig. 7). Therefore, H$_2$-Xe is actually the binary-gas mixture giving the smallest σ, since all mixtures with a larger $\mathcal{M}$ involve more internal degrees of freedom.

III. EXPERIMENTAL METHOD

A. Apparatus and gases

The apparatus was described in detail by de Bruyn *et al.* [8]. We used three convection cells with $\Gamma=30$ (cell 1:
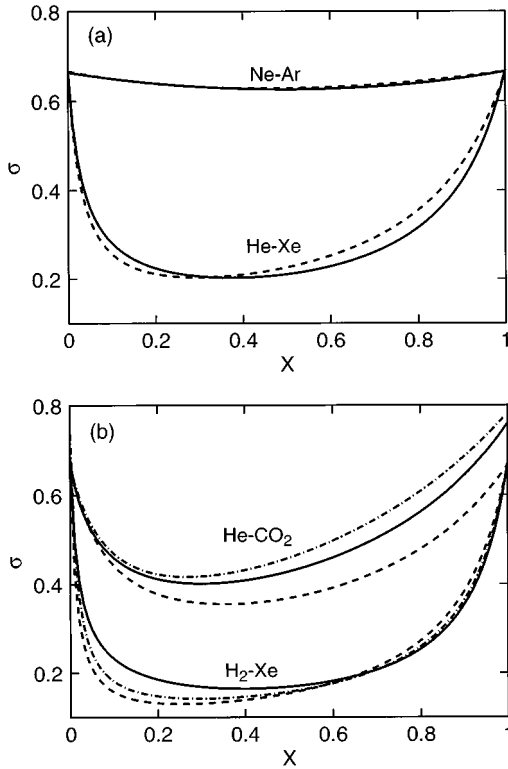
FIG. 10. Comparison of our best estimates (solid lines, $P=1$ bar and $T=25\,°C$) with the estimates based on the MFW approximation (dashed and dot-dashed lines). The dashed curves correspond to the approximation that all molecules are monatomic, while the dot-dashed curves take the internal degrees of freedom into account in the thermal conductivity and heat capacity. (a) Noble-gas mixtures Ne-Ar and He-Xe and (b) the mixtures He-CO_2 and H_2-Xe, which involve polyatomic molecules.

$r=43.2$ mm, $d=1.460$ mm), $\Gamma=29$ (cell 2: $r=43.0$ mm, $d=1.500$ mm), and $\Gamma=70$ (cell 3: $r=42.3$ mm, $d=0.608$ mm). They consisted of a sapphire top plate, a diamond-machined aluminum bottom plate, and circular sidewalls made of porous filter paper. The plates were parallel to within 2 μm. The pressure was regulated to ±0.005 bar. The top plate was held at a constant temperature T_t regulated to ±1 mK by circulating bath water, while the bottom-plate temperature T_b, regulated to ±0.5 mK, was varied as the experimental control parameter. The gas-filled volume outside the convection cell was filled with open-pore foam material to insulate the bottom plate and prevent convection.

All gases were purchased from Air Liquide America Corporation. Their purity was better than 99.99%. We used three pure gases (Ar, CO_2, and SF_6) and four binary-gas mixtures (Ne-Ar, He-CO_2, He-SF_6, and H_2-Xe) in convection experiments. By choosing different mixtures and pure gases and by varying their concentration and pressure, we varied σ from 0.17 to 1.01, Ψ from 0 to 0.80, $\mathcal{L}$ from 0.67 to 6.35, and Q from 0.07 to 4.51 (see Tables IV and V below). Three other pure gases (He, Ne, and N_2) were used as well to calibrate the heat conduction of the cell walls.

The H_2-Xe mixture was purchased from the manufacturer who specified the mole fraction of xenon to be $X=49.6\%$ with an accuracy of better than $\pm1\%$. The Ne-Ar,
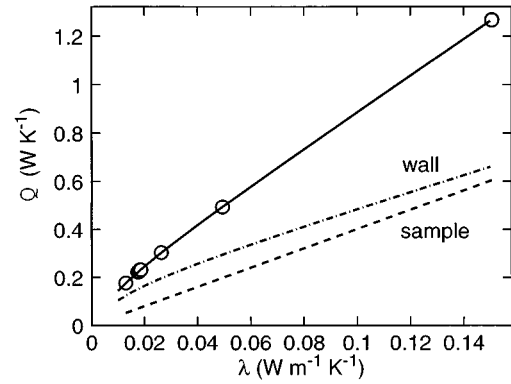

FIG. 11. Calibration of the thermal conductance $\mathcal{Q}(T_t,0)$ (in W/K) for cell 1 at $T_t=21.0\,°C$. From left to right, the circles are the experimental results for SF_6, CO_2, Ar, N_2, Ne, and He. The solid curve is a fit to the total conductance $\mathcal{Q}=0.1624 +7.427\lambda-1.0/(6.592+431.37\lambda)$. Here λ is in W/mK. The dashed and dot-dashed lines are the gas sample and wall conductance, respectively.

He-CO_2, and He-SF_6 mixtures were prepared in our laboratory from the pure gases. Before filling the mixing cylinder, we flushed it with the first component several times. After the cylinder was filled with the first component, the pressure P_1 and temperature T_1 were measured and the gas density was calculated from the equation of state. After the second component had been added, the final pressure P and temperature T were measured. The concentration was then determined from the mixture's equation of state by finding the value X that gives the correct density of the first component. The pressures and temperatures were always measured after thermal and concentration equilibrium was reached. To minimize the error from uncertainties in the equation of state (which is largest at the highest pressures), the final mixture pressure was kept as low as possible and yet high enough to fill the convection cell to the desired pressure of the experiment. The concentration accuracy of our mixtures was $\pm(1-2)$ %.

The onset of convection was determined by measuring the Nusselt number $\mathcal{N}$ and the shadowgraph-image contrast. By definition, $\mathcal{N}=1$ in the conduction state. As convection starts, $\mathcal{N}$ increases with ΔT because the heat transport is enhanced by convection. The convection modulates the temperature and concentration fields horizontally, leading to spatial variation of the vertical average of the refractive index in the x-y plane, which is visualized by the shadowgraph method [8,31].

B. Heat conduction of the cell wall

To measure the Nusselt number $\mathcal{N}$ and the thermal conductivity of the gas mixtures precisely, we calibrated the heat conduction of the cell sidewall using six pure gases (He, Ne, Ar, N_2, CO_2, and SF_6) with a wide range of known thermal conductivities. In the conduction state, the conductance (equal to the heat current per unit temperature difference) of the gas inside the cell is $\mathcal{Q}_g=A\lambda/d$, where $A=\pi r^2$ is the cell area. The conductance $\mathcal{Q}_w$ of the sidewall, foam, solid supports, and the gas outside the cell can be modeled as heat

TABLE III. Comparison of the thermal conductivities of binary-gas mixtures measured in this experiment (λ_m) with the ones calculated with our programs (λ_c).

Mixture	T (°C)	P (bars)	X	$100\lambda_m$ (W/mK)	$100\lambda_c$ (W/mK)	$100[(\lambda_m-\lambda_c)/\lambda_c]$
Ne-Ar	23.0	36.65	0.680	2.584	2.560	0.9
He-CO$_2$	21.0	30.60	0.537	4.888	4.730	3.3
He-CO$_2$	22.5	25.97	0.879	2.457	2.459	-0.1
He-SF$_6$	20.5	28.10	0.199	7.476	7.539	-0.8
He-SF$_6$	25.0	18.79	0.578	3.156	3.162	-0.2
He-SF$_6$	20.0	15.33	0.380	4.861	4.711	3.2
H$_2$-Xe	21.0	20.67	0.496	5.539	5.271	5.1
H$_2$-Xe	21.0	35.23	0.496	5.602	5.368	4.4

transport in porous media [91]. Then the total heat conductance $\mathcal{Q}=\mathcal{Q}_g+\mathcal{Q}_w$ can be expressed as

$$\mathcal{Q}=\frac{A\lambda}{d}+a_1\lambda+a_2-\frac{1}{a_3\lambda+a_4}, \qquad (31)$$

where a_1 to a_4 are positive and depend on the properties of the filter paper and foam, the geometry outside the cell, the thermal conductivity of solid supports, and so on. These fitting parameters are temperature dependent.

In the experiment, we kept the top-plate temperature T_t constant and increased the bottom-plate temperature T_b. This protocol caused the mean temperature $T_m=(T_t+T_b)/2$ and thus the average thermophysical properties and $\mathcal{Q}$ to vary with $\Delta T=T_b-T_t$ [92]. Furthermore, as ΔT changed, the mean concentration X_m inside the convection cell varied slightly because of the diffusion that resulted from the difference of the mean temperatures inside and outside the cell. The concentration variation also changed the properties and $\mathcal{Q}$. In short, when ΔT went up, T_m increased, while X_m decreased slightly for $\Psi>0$. For our mixtures, both increasing T_m and decreasing X_m raised the thermal conductivity, so $\mathcal{Q}$ increased with ΔT. In the conduction state, we have the linear relationship

$$\mathcal{Q}(T_t,\Delta T)=\mathcal{Q}_0(T_t)+\mathcal{Q}'(T_t)\Delta T \qquad (32)$$

for not very large ΔT and the thicker cells 1 ($d=1.460$ mm) and 2 ($d=1.500$ mm), as confirmed by the heat-transport measurement [see Fig. 12(a)]. The quantity $\mathcal{Q}'(T)$ turned out to be small. For the *thin* cell 3 ($d=0.608$ mm), however, we found that the quadratic term $\mathcal{Q}''(T_t)(\Delta T)^2$ had to be included in Eq. (32). Here $\mathcal{Q}''$ is negative and its absolute value is smaller than $\mathcal{Q}'$ by a factor of 20–100.

We calibrated the cell conduction at $T=T_t$ by extrapolating $\mathcal{Q}(T_t,\Delta T)$ to $\Delta T=0$. Figure 11 shows a calibration result for cell 1 at $T=21$ °C. The average deviation of the fitted curve [solid line, Eq. (31)] from the experimental data (circles) is about 0.4%. The cell contribution $\mathcal{Q}_g$ and the wall contribution $\mathcal{Q}_w$ are plotted as dashed and dot-dashed curves, respectively, in Fig. 11. We note that the cell wall conducts more than half of the heat. Similar results were obtained for the other cells.

C. The mean concentration for $\Delta T>0$

For $\Delta T>0$, the mean concentration X_m in the cell was slightly smaller than the initial value X_0 at $\Delta T=0$ because $\Psi>0$ and the mean temperature inside the cell was larger than that outside the cell. We obtained X_m by measuring $d\mathcal{Q}/dT_m=2(d\mathcal{Q}/d\Delta T)$ in the conduction state. One has

$$\frac{d\mathcal{Q}}{dT_m}=\frac{\partial\mathcal{Q}}{\partial\lambda}\frac{d\lambda}{dT_m}+\left(\frac{\partial\mathcal{Q}}{\partial T_m}\right)_\lambda \qquad (33)$$

and

$$\frac{d\lambda}{dT_m}=\left(\frac{\partial\lambda}{\partial T_m}\right)_X+\left(\frac{\partial\lambda}{\partial X}\right)_T\frac{dX}{dT_m}, \qquad (34)$$
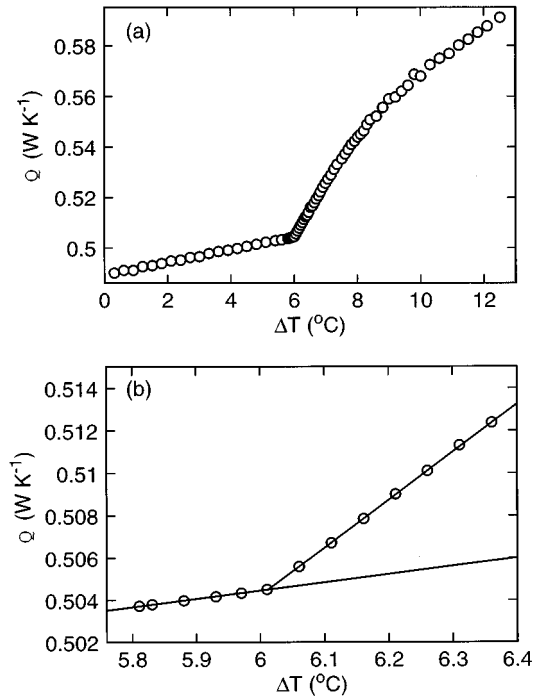
FIG. 12. Heat-transport measurement for a He-CO$_2$ mixture at $X=0.52$ and $P=30.6$ bars ($\Gamma=30$). (a) The total thermal conductance $\mathcal{Q}(\Delta T)$ for the whole range of ΔT in this experiment and (b) $\mathcal{Q}(\Delta T)$ near the onset of convection. Two solid lines in (b) are the linear fits to the data below and above the onset of convection, respectively. Their intersection gives the critical temperature difference $\Delta T_c=6.01$ °C.

TABLE IV. Primary experimental results. Cell 1, $d=1.460$ mm and $r=43.2$ mm; cell 2, $d=1.500$ mm and $r=43.0$ mm; cell 3, $d=0.608$ mm and $r=42.3$ mm. S_1^t and S_2^t are also listed here. See the text for notations.

Run	Cell	Gas	X_{mc}	P (bars)	T_{mc} (°C)	ΔT_c	S_1^e	S_1^t	S_2^e	S_2^t
1	2	H_2-Xe	0.49	20.67	25.83	9.65	0.37	0.71	0	-0.28
2	2	H_2-Xe	0.49	35.23	22.19	2.38	0.43	0.71	0	-0.32
3	1	He-SF_6	0.19	28.09	22.53	4.05	0.19	0.18	-0.17	-0.04
4	1	He-SF_6	0.38	15.33	22.96	5.92	0.49	0.79	-0.14	-0.49
5	1	He-SF_6	0.57	18.79	25.58	1.155	1.03	1.27	-0.75	-1.09
6	1	He-CO_2	0.50	20.29	30.30	18.6[a]				
7	1	He-CO_2	0.52	30.60	23.99	6.01	0.58	0.94	-0.13	-0.64
8	1	Ne-Ar	0.66	36.65	26.07	6.13	0.84	1.16	-0.10	-0.70
9	1	He-CO_2	0.87	25.97	23.33	1.67	1.11	1.40	-0.59	-1.23
10	1	Ar		29.73	23.45	4.89	1.08	1.41	-0.48	-1.25
11	1	SF_6		4.95	23.01	4.00	1.12	1.42	-0.52	-1.25
12	2	CO_2		13.81	23.29	4.58	1.12	1.42	-0.73	-1.25
13	1	CO_2		17.74	22.25	2.49	1.23	1.42	-1.04	-1.25
14	1	CO_2		24.92	21.46	0.920	1.21	1.42	-0.67	-1.25
15	2	CO_2		33.25	21.16	0.317	1.23	1.42	-0.98	-1.25
16	3	He-SF_6	0.35	35.85	26.54	11.08[a]				
17	3	He-SF_6	0.66	22.05	24.23	6.45				
18	3	He-CO_2	0.89	37.12	24.40	6.81[a]				
19	3	SF_6		13.64	23.87	3.68				
20	3	CO_2		33.84	22.86	4.71[a]				

[a]Non-Boussinesq case, hexagonal patterns appeared or coexisted with rolls for very small ϵ.

where $\lambda=\lambda(T_m)$ is the mean thermal conductivity. The value of $\partial\mathcal{Q}/\partial\lambda$ was calculated from Eq. (31), while $(\partial\lambda/\partial T_m)_X$ and $(\partial\lambda/\partial X)_T$ were evaluated from the thermal conductivity of the gas mixture. The quantity $(\partial\mathcal{Q}/\partial T_m)_\lambda$ is due to the temperature dependences of a_1 to a_4 in Eq. (31) and was determined in the calibration of the cell conduction. Assuming all quantities in Eqs. (33) and (34) to be constant, we get dX/dT_m from Eqs. (33) and (34) and thus $X_m=X_0+(dX/dT_m)\Delta T/2$. For $\Psi>0$, $dX/dT_m<0$.

D. Measurement of the thermal conductivity of the gas mixtures

The thermal conductivity λ of a gas mixture is determined from Eq. (31) by measuring $\mathcal{Q}$ with the gas mixture in the cell. The measured thermal conductivities λ_m and the calculated ones λ_c are given in Table III. The deviation $(\lambda_m-\lambda_c)/\lambda_c$ listed in the table results from the errors of the thermal conductivity measurement and the determination of the concentration. The latter affects λ_c.

The values of λ_m and λ_c agree well for Ne-Ar and He-CO_2 at $X=0.879$. The deviation of 3.3% for He-CO_2 at $X=0.537$ may be largely due to the concentration error since we know that the accuracy of λ_c is within 2% for He-CO_2 mixtures by comparing λ_c with independent experimental data in the literature (see the Appendix). If, for instance, $X=0.527$, then $\lambda_c=4.818\times10^{-2}$ W/mK, which is only 1.4% smaller than λ_m. For three He-SF_6 mixtures, the agreement is reasonably good, indicating that the approximate method due to Monchick *et al.* [71–73] is fairly accurate for this mixture. However, λ_m is more than 4% larger than λ_c for H_2-Xe. This deviation can only be partially at-

tributed to a concentration error since the concentration accuracy given by the manufacturer is $\pm1\%$. The difference may be largely due to the approximate nature of the method and the errors of the force constants for the Lennard-Jones potential [68]. In the remainder of this paper, we shall use λ_m for the H_2-Xe mixture and λ_c for the other five mixtures.

IV. EXPERIMENTAL RESULTS

A. Onset of convection

We determined the onset of convection for each gas or mixture by measuring the heat transport and the shadowgraph contrast. A typical example of heat-transport measurements is given in Fig. 12 for a run with a He-CO_2 mixture having an initial concentration $X=0.537$ ($P=30.60$ bars, run 7 in Tables IV and V). The top-plate temperature was fixed at $T_t=21.0$ °C, while the bottom-plate temperature T_b was increased in small steps from 21.0 °C to 33.5 °C. We allowed 2–6 h (over $2\Gamma^2 t_v$, where t_v is the vertical thermal diffusion time) at each ΔT for transients to decay before taking a time average of the total power p supplied to the bottom plate. Figure 12(a) gives the conductance $\mathcal{Q}=p/\Delta T$ versus ΔT for this run. When ΔT went up from zero, $\mathcal{Q}$ increased slowly and linearly in the conduction state. This increase is attributable primarily to the change in the mean concentration discussed in Sec. III C and to a lesser extent to the temperature dependence of gas conductivity and the wall conduction. At $\Delta T\approx6.0$ °C, $\mathcal{Q}$ started to grow faster, showing that convection occurred. An enlarged view of $\mathcal{Q}(\Delta T)$ near the onset of convection is given in Fig. 12(b). To find the critical temperature difference ΔT_c precisely, we fitted straight lines to the data below and above onset in Fig.

TABLE V. Dimensionless parameters and derived results for the experimental runs summarized in Table IV. See the text for notations.

Run	σ	$\mathcal{L}$	Ψ	Q	r_c^e	r_c^t	k_c^e	k_c^t
1	0.17	1.13	0.23	0.34	0.61	0.63	2.8	2.9
2	0.18	1.19	0.29	0.34	0.54	0.58	2.8	2.9
3	0.30	0.67	0.80	0.07	0.23	0.25	2.4	2.4
4	0.33	1.52	0.52	0.12	0.45	0.47	2.7	2.8
5	0.43	3.37	0.38	0.20	0.55	0.63	2.8	3.0
6	0.44	1.47	0.26	0.39	0.61	0.63	2.9	2.9
7	0.47	1.61	0.30	0.41	0.62	0.61	2.9	2.9
8	0.64	1.07	0.03	4.51	0.88	0.92	2.8	3.1
9	0.69	5.02	0.08	1.81	0.85	0.89	2.9	3.1
10	0.69		0		1.00	1.00	3.1	3.1
11	0.79		0		0.97	1.00	3.1	3.1
12	0.83		0		1.00	1.00	3.1	3.1
13	0.86		0		0.98	1.00	3.1	3.1
14	0.91		0		0.98	1.00	3.1	3.1
15	1.01		0		1.01	1.00	3.1	3.1
16	0.34	1.31	0.73	0.11	0.31	0.36	2.7	2.7
17	0.50	4.89	0.34	0.28	0.64	0.67	3.0	3.0
18	0.80	6.35	0.09	1.88	0.81	0.88	3.1	3.1
19	0.83		0		0.98	1.00	3.1	3.1
20	1.01		0		0.99	1.00	3.1	3.1

12(b). Their intersection gives $\Delta T_c = 6.01$ °C ± 0.01 °C. Results for ΔT_c obtained by this method are summarized in Table IV. There we also list the mean concentration X_{mc} and the mean temperature T_{mc} at onset. Experiments with pure gases are given in the table for comparison.

In the shadowgraph method [8,31], the initial (incoming) light intensity is $\mathcal{I}_0(\mathbf{x})$, where $\mathbf{x}$ is the horizontal position vector within the cell. The shadowgraph image at ΔT is denoted as $\mathcal{I}(\mathbf{x}, \Delta T)$. We define the shadowgraph signal as

$$I(\mathbf{x}, \Delta T) = \frac{\mathcal{I}(\mathbf{x}, \Delta T)}{\mathcal{I}_0(\mathbf{x})} - 1. \tag{35}$$

When there is no horizontal refractive-index variation, $I(\mathbf{x}, \Delta T) = 0$ if we neglect experimental noise. When convection occurs, the refractive index is modulated horizontally, and for small modulation $I(\mathbf{x}, \Delta T) \propto \delta n(\mathbf{x}, \Delta T)$ [8,31], where $\delta n(\mathbf{x}, \Delta T)$ is the vertical average of the deviation of the refractive index from its mean value. Figure 13 shows the spatial average $\langle I^2(\mathbf{x}, \Delta T)\rangle_{\mathbf{x}}$ of the square of the shadowgraph signal as a function of ΔT near the ones of convection for the experiment described in Fig. 12. For $\Delta T < \Delta T_c$, the small positive constant value of $\langle I^2 \rangle_{\mathbf{x}}$ (horizontal line in Fig. 13) is attributable to experimental noise. When $\Delta T > \Delta T_c$, there is an initially linear increase of $\langle I^2 \rangle_{\mathbf{x}}$ with ΔT as shown in Fig. 13. The critical temperature difference determined by the shadowgraph method is $\Delta T_c = 6.01$ °C ± 0.01 °C. The two methods giving the same ΔT_c demonstrates that the heat transport is enhanced significantly as soon as convection starts in binary-gas mixtures, similar to the case of pure fluids. In contrast, for *binary-liquid* mixtures with $\Psi > 0$, the
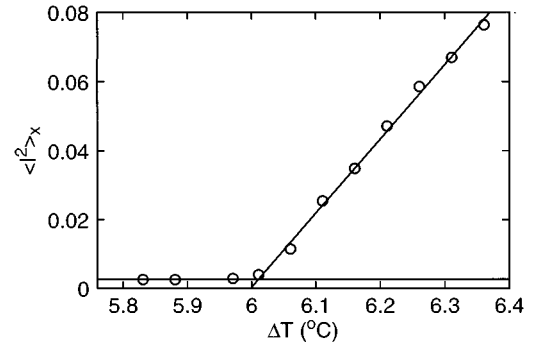

FIG. 13. Determination of ΔT_c by the shadowgraph method for the experiment in Fig. 12: $\langle I^2 \rangle_x$ as a function of ΔT. The data below ΔT_c are fitted to a horizontal line, while the data above ΔT_c are fitted to an inclined line. The intersection of the two lines gives $\Delta T_c = 6.01$ °C.

heat conduction is enhanced so little for $\Delta T_c < \Delta T < \Delta T_{c0}$ that ΔT_c cannot be determined by heat-transport measurements [30,31].

The convection patterns appearing at onset were rolls when ΔT_c was relatively small. Because of sidewall forcing [10,11], as ΔT increased from below to above ΔT_c, a concentric-roll (target) pattern appeared first [Fig. 14(a)]. It became unstable as

$$\epsilon \equiv \Delta T / \Delta T_c - 1 \tag{36}$$

increased [11]. After the target was completely destroyed at large ϵ, we reduced ΔT to just above ΔT_c. For relatively large Prandtl numbers ($\sigma \gtrsim 0.4$), time-independent straight-roll patterns were produced by this method at sufficiently small ϵ [Figs. 14(e) and 14(f)]. For smaller Prandtl numbers, the patterns appeared to be more susceptible to sidewall forcing. In that case straight-roll patterns occupied only part of the cell even at very small ϵ [Figs. 14(c) and 14(d)]. The remainder contained curved rolls more or less parallel to the sidewall. The patterns sometimes were slowly time dependent because defects generated near sidewall moved through the cell. Figures 14(c) and 14(d) were taken from the same run at a time interval of 56 min. When ϵ was increased slightly, a secondary instability led to time-dependent patterns with foci and defects [Fig. 14(b)] similar to those found in pure gases with $\sigma \simeq 1$ [5,12].

Hexagonal patterns appeared at onset in runs 6, 16, 18, and 20 (Table IV) because their ΔT_c was relatively large and the Oberbeck-Boussinesq approximation failed [2]. Figure 14(g) from a He-SF$_6$ mixture is similar to that found in pure CO$_2$ [93]. When ϵ was increased slightly, hexagons and rolls could coexist [Fig. 14(h)]. As ϵ was increased a little further, hexagons gave way completely to rolls.

The critical wave number k_c of the rolls at onset was calculated by Fourier analysis of the shadowgraph images. (The dimensionless wave number is defined as $k \equiv 2\pi d / \lambda_w$, where λ_w is the roll wavelength.) We found $k_c < k_{c0} = 3.117$ for convection in binary-gas mixtures (Table V), where k_{c0} is the critical wave number for convection in single-component fluids.

We calculated the critical Rayleigh number R_c and the critical wave number k_c based on the linear stability analysis
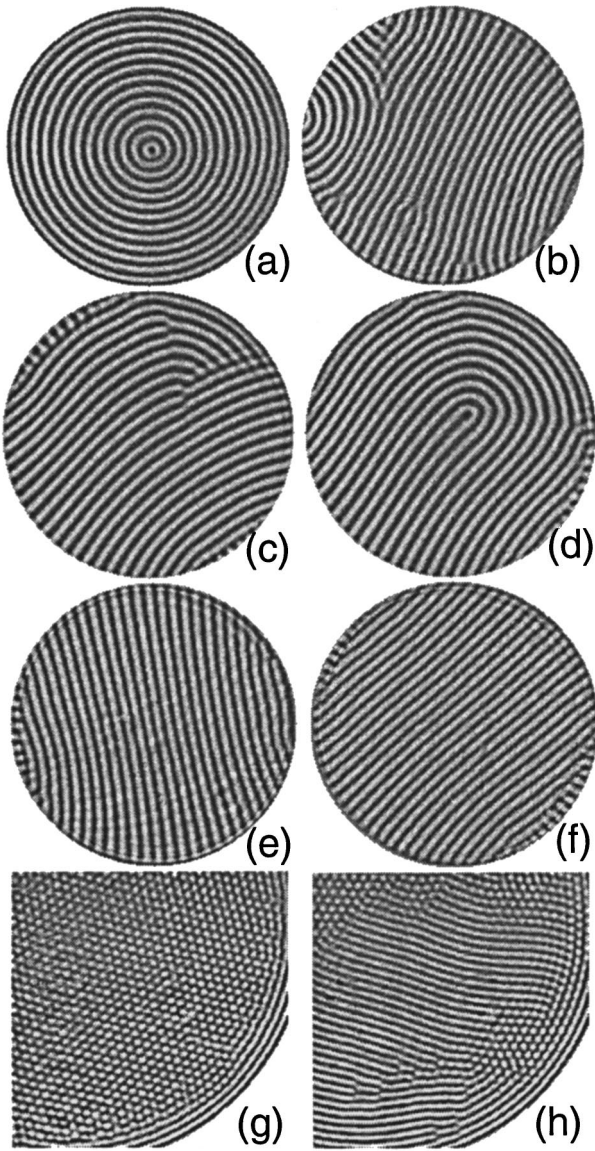
(a) (b) (c) (d) (e) (f) (g) (h)

FIG. 14. Convection patterns close to onset: (a) and (b) H_2-Xe at $X = 0.48, P = 20.7$ bars ($\sigma = 0.17$, $\Gamma = 29$), and (a) $\epsilon = 0.025$ and (b) $\epsilon = 0.046$; (c) and (d) He-SF$_6$ at $X = 0.38, P = 15.3$ bars ($\sigma = 0.33$, $\Gamma = 30$), and $\epsilon = 0.038$, and (d) was taken 56 min after (c) was imaged; (e) He-CO$_2$ at $X = 0.52, P = 30.6$ bars and $\epsilon = 0.055$ ($\sigma = 0.47$, $\Gamma = 30$); (f) pure CO$_2$ at $P = 24.92$ bars, $\epsilon = 0.043$ ($\sigma = 0.91$, $\Gamma = 30$); (g) and (h) He-SF$_6$ at $X = 0.35, P = 35.85$ bars ($\sigma = 0.34$, $\Gamma = 70$), and (g) $\epsilon = 0.012$ and (h) $\epsilon = 0.021$. For clarity, partial images are shown in (g) and (h).

of Hort, Linz, and Lücke [37] in order to compare the theory with our experiment, using a computer program provided by Hort and Lücke. The stability analysis takes both the Soret and Dufour effects into account. The calculations were done for the thermophysical properties at the mean temperature $T_{mc} = T_t + \Delta T_c/2$ and the mean concentration X_{mc} at the onset of convection.

In Table V we list the experimental results r_c^e and k_c^e for $r_c \equiv R_c/R_{c0} = \Delta T_c/\Delta T_{c0}^t$ and k_c for several mixtures, as well as the corresponding theoretical predictions r_c^t and k_c^t. The mean temperature T_{mc} and the mean concentration X_{mc} at onset were listed already in Table IV. In addition, we give
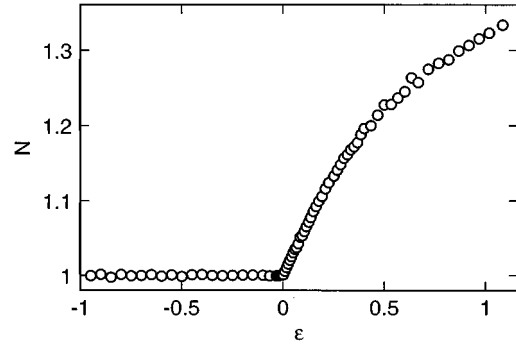

FIG. 15. Nusselt number as a function of ϵ for the experiment in Fig. 12.

the dimensionless numbers σ, Ψ, $\mathcal{L}$, and Q corresponding to these runs. The good agreement between experiment and theory for r_c and k_c shows that (i) the thermophysical properties are determined quite accurately and (ii) the evaluation of the linear stability analysis [37] is quite accurate. For most mixtures, r_c^e is a little smaller than r_c^t. This is probably due to the underestimation of the thermal diffusion ratio k_T and thus of Ψ at elevated pressures by considering only the second virial coefficient for k_T [Eq. (23)] (the thermal diffusion ratio depends strongly on pressure). This idea is consistent with the result for the two H_2-Xe mixtures (Table V); the run at the larger pressure has a larger relative difference between r_c^e and r_c^t.

B. The Nusselt number

We obtained the Nusselt numbers $\mathcal{N}$ from the conductance $\mathcal{Q}_g = \mathcal{Q} - \mathcal{Q}_w$ of the gas inside the cell. It is given by

$$\mathcal{N} = \frac{\mathcal{Q}_g(\Delta T)}{\mathcal{Q}_{g,cond}(\Delta T)} = \frac{\mathcal{Q}(\Delta T) - \mathcal{Q}_w(\Delta T)}{\mathcal{Q}_{g,cond}(\Delta T)}, \quad (37)$$

where the heat conductance of the gas in the absence of convection

$$\mathcal{Q}_{g,cond}(\Delta T) = \frac{A}{d}\left[\lambda(T_t) + 0.5\Delta T \frac{d\lambda}{dT}\right] \quad (38)$$

and the sidewall contribution

$$\mathcal{Q}_w(\Delta T) = \mathcal{Q}(T_t, \Delta T) - \mathcal{Q}_{g,cond}(\Delta T) \quad (39)$$

were determined from the heat-transport measurements in the conduction state [Eq. (32)] and the calibration of the sidewall conduction [Eq. (31)]. Their ΔT dependence was extrapolated to the convection state. Figure 15 shows $\mathcal{N}(\epsilon)$ for the measurements of $\mathcal{Q}(\Delta T)$ described in Fig. 12. In the conduction state ($\epsilon < 0$) $\mathcal{N} = 1$, while $\mathcal{N} > 1$ in the convection state.

Near the onset of convection, $\mathcal{N}$ can be expanded as

$$\mathcal{N} = 1 + S_1\epsilon + S_2\epsilon^2 + \cdots, \quad (40)$$

where S_1 and S_2 depend on σ, Ψ, Q, and $\mathcal{L}$. The coefficient S_1 is the initial slope of $\mathcal{N}(\epsilon)$ at onset and is given by

$$S_1 = \lim_{\epsilon \to 0+} (\mathcal{N} - 1)/\epsilon. \qquad (41)$$

The coefficient S_2 determines how $d\mathcal{N}/d\epsilon$ changes with ϵ near onset. We determined the slope S_1^e and S_2^e by a straight-line extrapolation at small ϵ of the experimental data for $(\mathcal{N} - 1)/\epsilon$ from $\epsilon > 0$ to $\epsilon = 0$. The results S_1^e and S_2^e for several runs are given in Table IV. The value of S_1^e is significantly larger than zero, in contrast to $S_1 \lesssim O(10^{-2})$ for convection in binary-liquid mixtures [30,31]. The quantity S_2^e is always negative, indicating that $\mathcal{N}$ increases more slowly as ϵ increases.

For pure fluids ($\Psi = 0$), the theoretical value $S_1^t(\sigma)$ for an infinitely extended pattern of perfect straight rolls was calculated exactly by Schlüter, Lortz, and Busse [94]. Although S_1 vanishes as σ goes to zero, the dependence on σ is weak for $\sigma \gtrsim 0.35$ and $S_1^t \simeq 1.42$ for $\sigma \simeq 1$. Such a calculation is not available for the mixtures ($\Psi > 0$). However, employing a low-order Galerkin approximation for nonslip, impermeable boundary conditions at the top and bottom of the cell, Hollinger and Lücke [38] derived an eight-mode Lorenz model that pertains when stationary straight rolls are stable close to onset. We evaluated the initial slope S_1^{HL} of $\mathcal{N}$ from this model for the parameters of our experimental runs. However, due to the approximate nature of the model [38,95,96], it gives $S_1^{HL} = 1.718$ independent of σ in the pure-fluid limit rather than the exact value 1.422 for σ near one. Thus we made the empirical but reasonable estimate $S_1^t \simeq (1.422/1.718)S_1^{HL}$. These values are compared with S_1^e in Table IV. They are found to be systematically higher than S_1^e by $0.2 - 0.3$. This difference between experiment and theory has long been known for pure fluids [97]. Presumably it is attributable to the depression of the heat transport in the experimental system by the boundaries, by roll curvature, and by defects in the pattern. We conclude that at best the difference $S_1^e(\Psi = 0) - S_1^e(\Psi)$ can be compared effectively with the corresponding theoretical prediction. Table IV suggests that the agreement for this difference is quite good.

It would seem instructive to examine S_1^e and S_1^t as a function of the dimensionless parameters that are relevant to the mixtures. Because, in principle, S_1 depends on Ψ, $\mathcal{L}$, σ, and Q, it is not very helpful to plot S_1 as a function of any one of these parameter. We illustrate this in Fig. 16(a), which shows S_1 as a function of Ψ. The results show no reasonable trend and scatter widely. Thus we searched for a parameter combination that would serve as an approximate scaling variable in the sense that the experimental and theoretical data for S_1, when plotted against this variable, will fall close to the same smooth curve. As already pointed out above, the σ dependence of S_1 is weak for pure fluids and $\sigma \gtrsim 0.35$. The eight-mode model shows [38] no dependence of S_1 on σ. Thus we neglected σ from the scaling variable. Examination of the eight-mode model's solutions [38] reveals that S_1 depends only very weakly on Q for the parameters of our experiments. Thus, to a good approximation Q may also be dropped. So finally we need an appropriate combination of Ψ and $\mathcal{L}$. Here we are guided by the analytic result for (unrealistic) permeable and free (slip) horizontal boundary conditions [98]
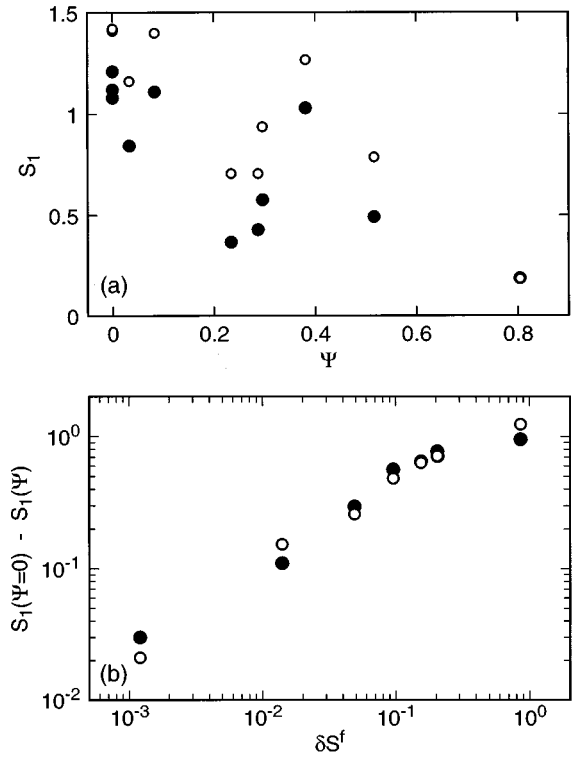

FIG. 16. Initial slope of the Nusselt number at onset. (a) S_1 as a function of Ψ and (b) S_1 as a function of δS^f [see Eq. (43)] on log-log scale. The experimental (theoretical) values are given by solid (open) circles.

$$S_1^f(\Psi, \mathcal{L}) = \frac{2[1 + \Psi(1 + \mathcal{L}^{-2})]}{1 + \Psi(1 + \mathcal{L}^{-2} + \mathcal{L}^{-3})}. \qquad (42)$$

However, for pure fluids, $S_1^f(\Psi = 0) = 2$, which is larger than the result of Schüler et al. for realistic rigid boundaries. Thus we examine only the difference $S_1^{e,t}(0) - S_1^{e,t}(\Psi, \mathcal{L})$ as a function of the scaling variable

$$\delta S^f = 2 - S_1^f(\Psi, \mathcal{L}). \qquad (43)$$

This is done in Fig. 16(b), where we used the average experimental value $S_1^e(0) = 1.14$ from the three pure gases and
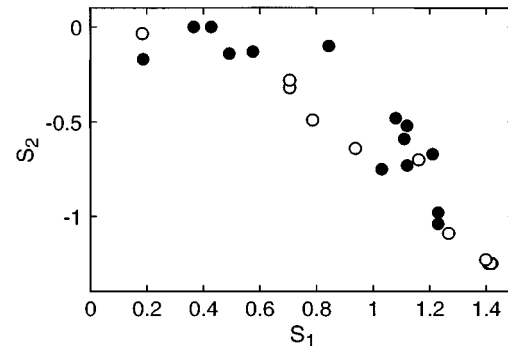

FIG. 17. Value of S_2^e (S_2^t) as a function of S_1^e (S_1^t). The experimental (theoretical) values are given by solid (open) circles.
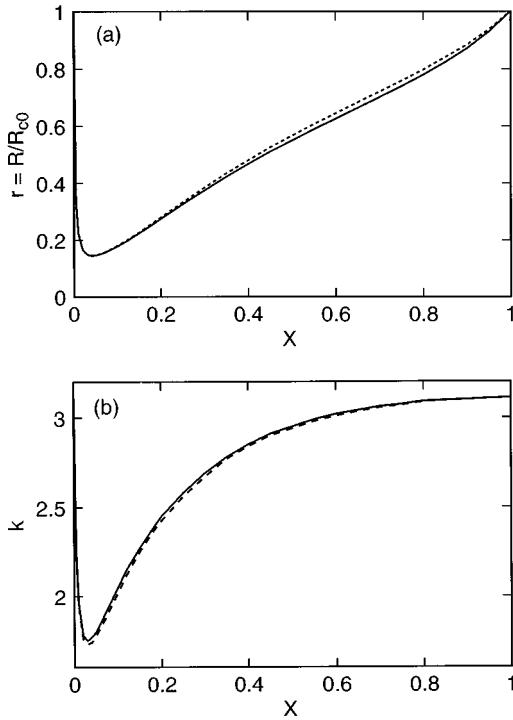
FIG. 18. Comparison of (a) r_c and (b) k_c for the onset of convection in a He-SF$_6$ mixture with (solid curves) and without (dashed curves) the Dufour effect. The conditions $P=22$ bars and $T=25\,°$C are the same as those in Fig. 8.

the prediction $S_1^t(0)=1.42$ of Schlüter *et al.* Both theory and experiment, to a very good approximation, fall on a single curve.

The theoretical value of S_2 was also estimated by using the eight-mode model for both pure gases and binary-gas mixtures. The correction factor discussed above was employed, so $S_2^t \simeq (1.422/1.718)S_2^{HL}$. The value of S_2^t is listed in Table IV for some experimental runs. In Fig. 17, S_2^e and S_2^t are plotted as a function of S_1^e and S_1^t, respectively. We find that S_2^e agrees with S_2^t, though both of them are quite scattered and a smooth curve does not seem to exist. There is a clear trend that S_2 decreases with increasing S_1, i.e., as ϵ increases $d\mathcal{N}/d\epsilon$ decreases more slowly for smaller initial slope $S_1=(d\mathcal{N}/d\epsilon)_{\epsilon=0+}$.

V. DISCUSSION

A. The strength of the Dufour effect

The influence of the Dufour effect ($Q>0$) depends on $\mathcal{L}Q\Psi$ and $\mathcal{L}Q\Psi^2$ [see Eq. (10)]. In Sec. II B we found that the values of these parameter combinations are small, for instance, for Ar-CO$_2$ ($P=22$ bars, $T=25\,°$C) even though Q itself is not small (Fig. 6). For He-SF$_6$ under the same conditions, $\mathcal{L}Q\Psi^2$ is also small, but $\mathcal{L}Q\Psi$ can be relatively large (Fig. 8). Thus we examine the linear properties of this mixture, using stability analysis [37]. In Fig. 18 we plot r_c and k_c for the He-SF$_6$ mixture with ($Q>0$, solid line) and without ($Q=0$, dashed line) the Dufour effect. The value of r_c increases very slightly when the Dufour effect is turned off, while k_c decreases by a small amount. The effect

is at most of the same size as typical experimental errors and much smaller than the Soret effect. The other four mixtures (Ne-Ar, He-CO$_2$, He-Xe, and H$_2$-Xe) show a similar or weaker Dufour effect.

B. Summary

In this paper we presented the results of an extensive experimental investigation of Rayleigh-Bénard convection in binary-gas mixtures. A complete set of thermodynamic and transport properties was accurately determined for six binary-gas mixtures (He-CO$_2$, He-SF$_6$, He-Xe, Ne-Ar, Ar-CO$_2$, and H$_2$-Xe) by a combination of fitting data in the literature, doing molecular-theory calculations, and measuring the thermal conductivity ourselves. All six mixtures have positive separation ratios $\Psi>0$ (Fig. 4). The Lewis number $\mathcal{L}$ is of order one (Fig. 5). An important feature of binary-gas mixtures is that their Prandtl number can be lower than that of the two pure components (Fig. 7). We discussed the physical reason and showed that the minimum Prandtl number that can be reached is about 0.16. Such low Prandtl numbers may be of technological importance in design engineering involving heating or refrigeration systems [50,90].

Both the heat-transport (Nusselt number $\mathcal{N}$) measurements and the shadowgraph imaging gave the same critical temperature difference ΔT_c for the onset of convection in binary-gas mixtures. The measured $r_c=R_c/R_{c0}$ and k_c (Table V) agree well with the prediction of linear stability analysis [37]. In contrast to convection in binary-liquid mixtures having $\Psi>0$, $\mathcal{N}$ increases significantly in binary-gas mixtures as soon as R_c is exceeded and convection starts. Consistent with predictions [35] for this parameter range, the convection patterns appearing near onset (Fig. 14) are rolls (hexagons appear at onset for relatively large ΔT_c). So the convection in binary-gas mixtures behaves qualitatively like that in pure fluids, except that $R_c<R_{c0}=1708$ and $k_c<k_{c0}=3.117$. The initial slope of the Nusselt number $(d\mathcal{N}/d\epsilon)_{\epsilon=0+}$ at onset was compared with that predicted by an eight-mode Galerkin truncation [38,96]. Good agreement was found for the variation of this slope with Ψ and $\mathcal{L}$ (Fig. 16). Based on the gas-mixture properties determined in this paper, we found that the Dufour effect (the reciprocal process of the Soret effect) is very weak in binary-gas convection (Fig. 18).

In view of the great variety of nonlinear phenomena found in binary-liquid mixtures with $\Psi<0$ [29], it would be interesting to study RBC in binary-gas mixtures with negative separation ratios. Gas mixtures can have lower Prandtl numbers, larger Lewis numbers, larger aspect ratios, and faster time scales than liquid mixtures. Unfortunately, it appears that the separation ratio is always positive for relatively low pressures. A negative Ψ can perhaps be found in the critical region [99] and in very dense gases [100]. However, it is hard to obtain a complete set of thermophysical properties under those conditions.

Although so far binary-gas mixtures have been limited to $\Psi>0$, they provide unique opportunities for the exploration of various nonlinear phenomena in RBC at Prandtl numbers between 0.16 and 1 and for Lewis numbers of order one. An important example is high-Rayleigh-number turbulent convection [7], where the nature of the boundary layers should

change as Ψ, σ, and $\mathcal{L}$ are varied. Another is the quantita-
tive study of the effect of σ and $\mathcal{L}$ on various secondary
instabilities and spatiotemporal chaos. Using gas mixtures,
we found recently that the onset of spiral-defect chaos de-
pends significantly on the Prandtl number [25]. A detailed
study of complex spatiotemporal behavior of convection pat-
terns will be presented in another paper of this series [51].

ACKNOWLEDGMENTS

APPENDIX

Here we give major references for each gas and mixture.
The actual methods used to obtain the thermophysical prop-
erties are briefly described. Since a large number of theoret-
ical and fitting equations are involved, we do not reproduce
them here.

1. Pure gases

a. CO_2

A precise high-order expansion for the equation of state is
given by Vukalovich and Altunin [55]. Fits of suitable equa-
tions to data for η and λ are summarized by de Bruyn *et al.*
[8]. The specific heat C_p is tabulated in Ref. [55].

b. He

The equation of state is given by Tsederberg *et al.* [52] up
to the third virial coefficient. These authors also give C_p and
fits to η and λ. Some of their fits were cross-checked by
experimental data from Ref. [101].

c. Ne and Ar

The second virial-coefficient B, zero-density η, and zero-
density λ were calculated from kinetic theory [59]. The den-
sity dependences of η and λ were obtained from fits to the
data in Ref. [53]. The heat capacity C_p is based on the data
in Ref. [53]. We cross-checked the various estimates using
the experimental data in Refs. [102,103].

d. Xe

All fits for B, η, λ, and C_p are based on the data in Ref.
[53]. Some of the fitting equations are given in that book. We
cross-checked some results using the experimental data from
Ref. [103].

e. N_2

Our estimate of the second virial-coefficient B is based on
a fit to the data in Ref. [60]. The estimates of the zero-
density η and λ are fits to the data in Ref. [60] and in Ref.
[104], respectively. Their density dependence was obtained

from a fit to the data in Ref. [105] and in Ref. [106], respec-
tively. For the heat capacity C_p we used a fit to the data in
Ref. [54].

f. H_2 (normal hydrogen)

The second virial-coefficient B was obtained from a fit to
the data in Refs. [63,107]. The zero-density η and λ are from
fits to the data in Ref. [83]. The density dependence of η is
from a fit to the data of Ref. [105], while the density depen-
dence of λ is from Ref. [108]. The heat capacity C_p is a fit to
the data from Ref. [54].

g. SF_6

The equation of state is given in Ref. [109] up to the
eighth virial coefficient. Equations for the thermal conduc-
tivity λ are given in Ref. [110] and the equations for η are
given in Ref. [111]. The heat capacity C_p at atmospheric
pressure is a fit to the data in Ref. [104] and its pressure
dependence is a fit to the data in Ref. [112].

2. Binary-gas mixtures

a. Ne-Ar

The second virial coefficient B and zero-density
η, λ, D, and k_T were calculated from statistical-
mechanical theory [59]. We took the density dependence of
η from that of the two pure components [53], while the
density dependence of λ was obtained by fitting to the data
in Refs. [53,85]. No data are available for the pressure de-
pendence of D and k_T, so the models discussed in Sec. II A3
were used to estimate their pressure dependence. We cross-
checked some of the results using the data in Refs.
[81,85,89,102].

b. He-Xe

The second virial coefficient B and zero-density
η, λ, D, and k_T were calculated by statistical-mechanical
theory [59]. The density dependence of η and λ was ob-
tained from the two pure components [53,103]. No data are
available for the pressure dependence of D and k_T, so the
models discussed in Sec. II A3 were used to estimate their
pressure dependence. Some of these results were cross-
checked by the data in Refs. [78,113–115].

c. He-CO_2

An equation of state containing up to the fifth virial coef-
ficient was used. The second virial coefficient B was fitted to
the data in Refs. [64,116]. The third virial coefficient C was
fitted to the data at $0\,°C$ [116] using the formula
$C = C_{he}X_{he} + C_c X_c^a$. Here a is the fitting parameter. The
fourth and fifth virial coefficients were estimated from that of
pure CO_2 neglecting helium, i.e., $D = D_c X_c^4$ and $E = E_c X_c^5$.
For the zero-density η and λ, Eq. (21) was fitted to the
experimental data in Refs. [79,84]. Their density dependence
was obtained from a fit to the data in Refs. [79,84]. The
zero-density D and k_T were calculated from kinetic theory
[61]. The pressure dependence of k_T is given in Ref. [76] up
to 5 atm, while the pressure dependence of D was estimated

from the model discussed in Sec. II A3. The results for D and k_T were cross-checked by the data in Refs. [76,87,117–119].

d. Ar-CO$_2$

An equation of state containing terms up to the fifth virial coefficient was used. The second virial coefficient B was fitted to the experimental data in Ref. [66]. The third coefficient was based on pure Ar [120] and CO2 [55]. The fourth and fifth coefficients were based on those of pure CO_2 alone. We fitted Eq. (21) for the zero-density η and λ to the experimental data in Refs. [121,122] and in Ref. [84], respectively. The pressure dependence of η was taken from that of the pure components, while the pressure dependence of λ was fitted to the data from Ref. [84]. The zero-density D and k_T were calculated by kinetic theory [61]. The pressure dependence of k_T was estimated from the result on p. 617 of Ref. [32]. The pressure dependence of D was evaluated from the model discussed in Sec. II A3.

e. He-SF$_6$

We used an equation of state containing terms up to the fourth virial coefficient. The second virial coefficient B was calculated from kinetic theory except that B_{12} was corrected using the data from Refs. [64,65]. The third virial coefficient

was based on the two pure components, while the fourth virial coefficient was estimated from pure SF$_6$. The zero-density η was calculated from kinetic theory [61], while the zero-density λ was estimated by the approximate method due to Monchick et al. (see Sec. II A2). The pressure dependence of η and λ was taken from that of the two pure gases. The zero-density D and k_T were also calculated from kinetic theory [61]. However, we corrected k_T based on the experimental data in Refs. [76,86,87] since the calculated values were systematically smaller than the experimental data. The pressure dependence of D is given up to 9 atm at 300 K by Ref. [75], while the pressure dependence of k_T is given by Ref. [76] up to 5 atm.

f. H$_2$-Xe

The second virial coefficient was determined from Refs. [53,63,107]. The zero-density η was calculated from kinetic theory based on a Lennard-Jones potential [68]. The zero-density λ was estimated by the method of Monchick et al. The density dependence of η and λ was based on that of the pure gases. The zero-density D and k_T were calculated from kinetic theory [68]. Their density dependence was estimated from the models discussed in Sec. II A3. Some theoretical results were cross-checked by the data in Refs. [78,82,88,123].

[1] A large amount of literature on Rayleigh-Bénard convection has evolved. For a discussion of linear stability see S. Chandrasekhar, *Hydrodynamic and Hydromagnetic Stability* (Oxford University Press, London, 1961). A review of early experimental work is given by E. L. Koschmieder, Adv. Chem. Phys. **26**, 177 (1974). More recent reviews of various aspects of RBC can be found in Refs. [2–8].

[2] F. H. Busse, Rep. Prog. Phys. **41**, 1929 (1978).

[3] F. H. Busse, in *Hydrodynamic Instabilities and the Transition to Turbulence*, edited by H. L. Swinney and J. P. Gollub (Springer, Berlin, 1981).

[4] R. P. Behringer, Rev. Mod. Phys. **57**, 657 (1985).

[5] V. Croquette, Contemp. Phys. **30**, 113 (1989); **30**, 153 (1989).

[6] For a comprehensive recent review see M. C. Cross and P. C. Hohenberg, Rev. Mod. Phys. **65**, 851 (1993).

[7] E. D. Siggia, Annu. Rev. Fluid Mech. **26**, 137 (1994).

[8] J. R. de Bruyn, E. Bodenschatz, S. W. Morris, S. P. Trainoff, Y. Hu, D. S. Cannell, and G. Ahlers, Rev. Sci. Instrum. **67**, 2043 (1996).

[9] R. Krishnamurti, J. Fluid Mech. **42**, 295 (1970); **42**, 309 (1970).

[10] V. Steinberg, G. Ahlers, and D. S. Cannell, Phys. Scr. **T9**, 97 (1985).

[11] Y.-C. Hu, R. E. Ecke, and G. Ahlers, Phys. Rev. E **48**, 4399 (1993).

[12] Y.-C. Hu, R. E. Ecke, and G. Ahlers, Phys. Rev. E **51**, 3263 (1995).

[13] R. M. Clever and F. H. Busse, J. Fluid Mech. **65**, 625 (1974).

[14] F. H. Busse and R. M. Clever, J. Fluid Mech. **91**, 319 (1979).

[15] E. W. Bolton, F. H. Busse, and R. M. Clever, J. Fluid Mech. **164**, 469 (1986).

[16] For early work on the irregular time dependence of convection patterns at R slightly above R_c see, for instance, G. Ahlers, Phys. Rev. Lett. **33**, 1185 (1974); G. Ahlers and R. P. Behringer, *ibid.* **40**, 712 (1978); M. S. Heutmaker, P. N. Fraenkel, and J. P. Gollub, *ibid.* **54**, 1369 (1985); G. Ahlers, D. S. Cannell, and V. Steinberg, *ibid.* **54**, 1373 (1985); A. Pocheau, V. Croquette, and P. Le Gal, *ibid.* **55**, 1094 (1985).

[17] S. W. Morris, E. Bodenschatz, D. S. Cannell, and G. Ahlers, Phys. Rev. Lett. **71**, 2026 (1993).

[18] S. W. Morris, E. Bodenschatz, D. S. Cannell, and G. Ahlers, Physica D **97**, 164 (1996).

[19] A. Libchaber and J. Maurer, J. Phys. (Paris) Colloq. **41**, C3-51 (1978).

[20] H. D. I. Abarbanel, R. Brown, J. J. Sidorowich, and L. S. Tsimring, Rev. Mod. Phys. **65**, 1331 (1993).

[21] M. Assenheimer and V. Steinberg, Phys. Rev. Lett. **70**, 3888 (1993).

[22] M. Assenheimer and V. Steinberg, Nature **367**, 345 (1994).

[23] Y.-C. Hu, R. E. Ecke, and G. Ahlers, Phys. Rev. Lett. **74**, 391 (1995).

[24] M. C. Cross and P. C. Hohenberg, Science **263**, 1569 (1994).

[25] J. Liu and G. Ahlers, Phys. Rev. Lett. **77**, 3126 (1996).

[26] A. Oberbeck, Ann. Phys. Chem. **7**, 271 (1879).

[27] J. Boussinesq, *Théorie Analytique de la Chaleur* (Gauthier-Villars, Paris, 1903), Vol. 2.

[28] F. Busse, J. Fluid Mech. **30**, 625 (1967).

[29] The references to experimental work on binary-liquid mixtures are too numerous to all be listed here. A recent sum-

mary has been given in Ref. [6]. For some of the original work with *negative* separation ratios see R. W. Walden, P. Kolodner, A. Passner, and C. M. Surko, Phys. Rev. Lett. **55**, 496 (1985); I. Rehberg and G. Ahlers, *ibid.* **55**, 500 (1985); E. Moses, J. Fineberg, and V. Steinberg, Phys. Rev. A **35**, 2757 (1987); R. Heinrichs, G. Ahlers, and D. S. Cannell, *ibid.* **35**, 2761 (1987); J. J. Niemela, G. Ahlers, and D. S. Cannell, Phys. Rev. Lett. **64**, 1365 (1990); P. Kolodner, J. A. Glazier, and H. Williams, *ibid.* **65**, 1579 (1990); K. Lerman, E. Bodenschatz, D. S. Cannell, and G. Ahlers, *ibid.* **70**, 3572 (1993).

[30] E. Moses and V. Steinberg, Phys. Rev. A **43**, 707 (1991).

[31] M. A. Dominguez-Lerma, G. Ahlers, and D. S. Cannell, Phys. Rev. E **52**, 6159 (1995).

[32] J. O. Hirschfelder, C. F. Curtiss, and R. B. Bird, *Molecular Theory of Gases and Liquids* (Wiley, New York, 1964).

[33] Thermal diffusion is the mass diffusion induced by a temperature gradient, while the ordinary mass diffusion results from concentration gradients. However, the term ''thermal diffusion time'' denotes the characteristic time of temperature relaxation due to thermal conduction.

[34] See p. 519 of Ref. [32].

[35] T. Clune and E. Knobloch, Phys. Rev. A **44**, 8084 (1991).

[36] S. R. de Groot and P. Mazur, *Non-Equilibrium Thermodynamics* (North-Holland, Amsterdam, 1962), Chap. 11.

[37] W. Hort, S. J. Linz, and M. Lücke, Phys. Rev. A **45**, 3737 (1992).

[38] St. Hollinger and M. Lücke, Phys. Rev. E **52**, 642 (1995).

[39] L. D. Landau and E. M. Lifshitz, *Fluid Mechanics* (Pergamon, London, 1959).

[40] S. J. Linz, Phys. Rev. A **40**, 7175 (1989).

[41] S. J. Linz, Phys. Rev. E **49**, 5881 (1994).

[42] A. Zippelius and E. D. Siggia, Phys. Fluids **26**, 2905 (1983).

[43] E. D. Siggia and A. Zippelius, Phys. Rev. Lett. **47**, 835 (1981); M. C. Cross and A. C. Newell, Physica D **10**, 299 (1984); H. S. Greenside, M. C. Cross, and W. M. Coughran, Jr., Phys. Rev. Lett. **60**, 2269 (1988).

[44] H.-W. Xi, J. D. Gunton, and J. Viñals, Phys. Rev. Lett. **71**, 2030 (1993).

[45] M. Bestehorn, M. Fantz, R. Friedrich, and H. Haken, Phys. Lett. A **174**, 48 (1993).

[46] V. Croquette, P. Le Gal, A. Pocheau, and R. Guglielmetti, Europhys. Lett. **1**, 393 (1986).

[47] F. Daviaud and A. Pocheau, Europhys. Lett. **9**, 7 (1989).

[48] See pp. 16 and 527 of Ref. [32].

[49] An exception is liquid helium. As the superfluid-transition temperature 2.176 K is approached from above, σ vanishes. However, experiments are difficult because σ varies from a value of order one to zero over a narrow temperature range of a few mK and because of the problem of flow visualization, which has only recently been achieved under the required cryogenic conditions [A. L. Woodcraft, P. G. J. Lucas, R. G. Matley, and Y. T. Wong, Czech. J. Phys. **46**, 85 (1996)].

[50] F. W. Giacobbe, J. Acoust. Soc. Am. **96**, 3568 (1994).

[51] J. Liu and G. Ahlers (unpublished).

[52] N. V. Tsederberg, V. N. Popov, and N. A. Morozova, *Thermodynamic and Thermophysical Properties of Helium* (Israel Program for Scientific Translations, Jerusalem, 1971).

[53] V. A. Rabinovich, A. A. Vasserman, V. I. Nedostup, and L. S. Veksler, *Thermophysical Properties of Neon, Argon, Krypton, and Xenon* (Hemisphere, Washington, DC, 1988).

[54] J. Hilsenrath, H. J. Hoge, C. W. Beckett, J. F. Masi, W. S. Benedict, R. L. Nuttall, L. Fano, Y. S. Touloukian, and H. W. Woodlley, *Tables of Thermodynamic and Transport Properties of Air, Carbon Dioxide, Carbon Monoxide, Hydrogen, Nitrogen, Oxygen, and Steam* (Pergamon, New York, 1960).

[55] M. P. Vukalovich and V. V. Altunin, *Thermophysical Properties of Carbon Dioxide* (Collets, London, 1968).

[56] K. Stephan and T. Heckenberger, *Thermal Conductivity and Viscosity Data of Fluid Mixtures* (DECHEMA, Frankfurt am Main, 1988), Vol. 10, Pt. 1.

[57] See the references cited in Refs. [59,61].

[58] J. Kestin, S. T. Ro, and W. A. Wakeham, Physica **58**, 165 (1972); B. Najafi, E. A. Mason, and J. Kestin, Physica A **119**, 387 (1983).

[59] J. Kestin, K. Knierim, E. A. Mason, B. Najafi, S. T. Ro, and M. Waldman, J. Phys. Chem. Ref. Data **13**, 229 (1984).

[60] A. Boushehri, J. Bzowski, J. Kestin, and E. A. Mason, J. Phys. Chem. Ref. Data **16**, 445 (1987).

[61] J. Bzowski, J. Kestin, E. A. Mason, and F. J. Uribe, J. Phys. Chem. Ref. Data **19**, 1179 (1990).

[62] J. H. Dymond and E. B. Smith, *The Virial Coefficients of Pure Gases and Mixtures, A Critical Compilation* (Clarendon, Oxford, 1980).

[63] S. Pérez, H. Schmiedel, and B. Schramm, Z. Phys. Chem. Neue Folge **123**, S35 (1980).

[64] T. N. Bell and P. J. Dunlop, Chem. Phys. Lett. **84**, 99 (1981).

[65] M. L. Martin, R. D. Trengove, K. R. Harris, and P. J. Dunlop, Ber. Bunsenges. Phys. Chem. **86**, 626 (1982).

[66] T. N. Bell, C. M. Bignell, and P. J. Dunlop, Physica A **181**, 221 (1992).

[67] V. Vesovic, W. A. Wakeham, G. A. Olchowy, J. V. Sengers, J. T. R. Watson, and J. Millat, J. Phys. Chem. Ref. Data **19**, 763 (1990).

[68] See Chap. 8 and Appendix (Tables) of Ref. [32].

[69] R. C. Reid, J. M. Prausnitz, and T. K. Sherwood, *The Properties of Gases and Liquids*, 3rd ed. (McGraw-Hill, New York, 1977).

[70] V. K. Bammert and R. Klein, Atomkernenergie **26**, 217 (1975).

[71] L. Monchick, K. S. Yun, and E. A. Mason, J. Chem. Phys. **39**, 654 (1963).

[72] L. Monchick, A. N. G. Pereira, and E. A. Mason, J. Chem. Phys. **42**, 3241 (1965).

[73] J. Kestin and W. A. Wakeham, Int. J. Thermophys. **4**, 295 (1983).

[74] G. R. Staker and P. J. Dunlop, Chem. Phys. Lett. **42**, 419 (1976).

[75] T. N. Bell, I. R. Shankland, and P. J. Dunlop, Chem. Phys. Lett. **45**, 445 (1977).

[76] R. D. Trengove, H. L. Robjohns, M. L. Martin, and P. J. Dunlop, Physica A **108**, 502 (1981).

[77] R. M. Sevast'yanov, N. A. Zykov, and K. I. Voroshilova, Inzh. Fiz. Zh. **49**, 284 (1985) [J. Eng. Phys. **49**, 967 (1985)].

[78] K. P. Srivastava, J. Chem. Phys. **28**, 543 (1958).

[79] R. DiPippo, J. Kestin, and K. Oguchi, J. Chem. Phys. **46**, 4758 (1967).

[80] J. Kestin, H. E. Khalifa, S. T. Ro, and W. A. Wakeham, Physica A **88**, 242 (1977).

[81] J. Kestin, W. Wakeham, and K. Watanabe, J. Chem. Phys. **53**, 3773 (1970).

[82] S. C. Saxena and P. K. Tondon, J. Chem. Eng. Data **16**, 212 (1971).

[83] M. J. Assael, S. Mixafendi, and W. A. Wakeham, J. Phys. Chem. Ref. Data **15**, 1315 (1986).

[84] J. Kestin, Y. Nagasaka, and W. A. Wakeham, Physica A **113**, 1 (1982).

[85] A. A. Clifford, R. Fleeter, J. Kestin, and W. A. Wakeham, Physica A **98**, 467 (1979).

[86] P. J. Dunlop and C. M. Bignell, Ber. Bunsenges. Phys. Chem. **99**, 77 (1995).

[87] R. D. Trengove, H. L. Robjohns, and P. J. Dunlop, Physica A **128**, 486 (1984).

[88] P. J. Dunlop, H. L. Robjohns, and C. M. Bignell, J. Chem. Phys. **86**, 2922 (1987).

[89] A. F. Zolotukhina, M. V. Sagarda, E. A. Shashkov, and I. P. Evmenova, Inzh. Fiz. Zh. **49**, 810 (1985) [J. Eng. Phys. **49**, 1330 (1985)].

[90] G. W. Swift, Phys. Today **48** (7), 22 (1995).

[91] J. Bear, *Dynamics of Fluids in Porous Media* (Dover, New York, 1988).

[92] We can keep the mean temperature T_m inside the convection cell constant by decreasing the top-plate (or water bath) temperature T_t while increasing the bottom-plate temperature T_b. However, the variation of the bath temperature changes the strain on the cell holder surrounded by the bath water, leading to a slight shift of the shadowgraph image and to considerable difficulties in image processing. Furthermore, keeping T_m constant does not prevent the variation of X_m since the mean temperature outside the cell would be affected by the bath temperature.

[93] E. Bodenschatz, J. R. de Bruyn, G. Ahlers, and D. S. Cannell, Phys. Rev. Lett. **67**, 3078 (1991).

[94] A. Schlüter, D. Lortz, and F. Busse, J. Fluid Mech. **23**, 129 (1965).

[95] J. Niederländer, M. Lücke, and M. Kamps, Z. Phys. B **82**, 135 (1991).

[96] The Nusselt number given by Ref. [38] was evaluated at the top and bottom plates. The Galerkin model for rigid boundaries gives a laterally averaged heat flux that varies slightly as a function of the vertical coordinate [95]. Thus the heat currents at the two plates are larger than the vertical mean value. A better value for comparison with the exact $\Psi=0$ result of Schlüter *et al.* [94] would be a vertically and laterally averaged heat current from the eight-mode model. Then one gets $S_1 = 1.477$ for $\Psi=0$ [St. Hollinger and M. Lücke (private communication)], closer to the value 1.422 of Schlüter *et al.* However, a computation of this average is somewhat involved and requires the vertical eigenfunctions of the model. Thus, for $\Psi>0$ we used a more empirical procedure to force S_1 of the eight-mode model to agree with the exact result in the $\Psi=0$ limit. It simply consisted of multiplying S_1 by a Ψ-independent factor equal to $1.422/1.718$.

[97] For example, C. W. Meyer, G. Ahlers, and D. S. Cannell [Phys. Rev. A **44**, 2514 (1991)] found $1/g_3 \equiv S_1^e = 1.20$ [see below Eq. (2.8) of their paper] in a sample with $\sigma = 6.0$ and $\Gamma = 10$. This can be compared with the average value of 1.14 for our pure gases. We would not expect the two experimental values to agree precisely because of the different σ and Γ.

[98] H. R. Brand, P. C. Hohenberg, and V. Steinberg, Phys. Rev. A **30**, 2548 (1984).

[99] N. C. Pierce, R. B. Duffield, and H. G. Drickamer, J. Chem. Phys. **18**, 950 (1950).

[100] J. E. Walther and H. G. Drickamer, J. Phys. Chem. **62**, 421 (1958).

[101] M. Mustafa, M. Ross, R. D. Trengove, W. A. Wakeham, and M. Zalaf, Physica A **141**, 233 (1987).

[102] J. Kestin, Ö. Korfall, J. V. Sengers, and B. Kamgar-Parsi, Physica A **106**, 415 (1981).

[103] J. Kestin, R. Paul, A. A. Clifford, and W. A. Wakeham, Physica A **100**, 349 (1980).

[104] F. J. Uribe, E. A. Mason, and J. Kestin, J. Phys. Chem. Ref. Data **19**, 1123 (1990).

[105] J. A. Gracki, G. P. Flynn, and J. Ross, J. Chem. Phys. **51**, 3856 (1969).

[106] A. A. Clifford, J. Kestin, and W. A. Wakeham, Physica A **97**, 287 (1979).

[107] R. Artym and M. Kliem, Ber. Bunsenges. Phys. Chem. **95**, 1274 (1991).

[108] A. A. Clifford, P. Gary, A. I. Johns, A. C. Scott, and J. T. R. Watson, J. Chem. Soc. Faraday Trans. I **77**, 2679 (1981).

[109] A. Oda, M. Uematsu, and K. Watanabe, Bull. JSME **26**, 1590 (1983).

[110] J. Kestin and N. Imaishi, Int. J. Thermophys. **6**, 107 (1985).

[111] J. H. B. Hoogland, H. R. Van den Berg, and N. J. Trappeniers, Physica A **134**, 169 (1985).

[112] W. Braker and A. L. Mossman, *The Matheson Unabridged Gas Data Book: A Compilation of Physical and Thermodynamic Properties of Gases* (Matheson Gas Products, East Rutherford, NJ, 1974).

[113] J. Kestin, H. E. Khalifa, and W. A. Wakeham, Physica A **90**, 215 (1978).

[114] J. M. Gandhi and S. C. Saxena, J. Chem. Eng. Data **13**, 357 (1968); Mol. Phys. **12**, 57 (1967).

[115] W. L. Taylor, J. Chem. Phys. **72**, 4973 (1980).

[116] V. K. Bammert and R. Klein, Atomkernenergie **24**, 150 (1974).

[117] J. M. Symons, M. L. Martin, and P. J. Dunlop, J. Chem. Soc. Faraday Trans. I **75**, 621 (1979).

[118] J. N. Holsen and M. R. Strunk, I&EC Fundam. **3**, 143 (1964).

[119] R. D. Trengove, K. R. Harris, H. L. Robjohns, and P. J. Dunlop, Physica A **131**, 506 (1985).

[120] M. Orentlicher and J. M. Prausnitz, Can. J. Chem. **45**, 373 (1970).

[121] J. Kestin and S. T. Ro, Ber. Bunsenges. Phys. Chem. **80**, 619 (1976).

[122] A. Hobley, G. P. Matthews, and A. Townsend, Int. J. Thermophys. **10**, 1165 (1989).

[123] P. J. Dunlop, Physica A **145**, 597 (1987).